

1 **Long-term MAX-DOAS network observations of NO<sub>2</sub> in Russia and Asia**  
2 **(MADRAS) during 2007–2012: instrumentation, elucidation of climatology, and**  
3 **comparisons with OMI satellite observations and global model simulations**

4  
5 **Y. Kanaya<sup>1</sup>, H. Irie<sup>1,\*</sup>, H. Takashima<sup>1,\*\*</sup>, H. Iwabuchi<sup>1,\*\*\*</sup>, H. Akimoto<sup>1,\*\*\*\*</sup>, K. Sudo<sup>2</sup>,**  
6 **M. Gu<sup>3</sup>, J. Chong<sup>3</sup>, Y. J. Kim<sup>3</sup>, H. Lee<sup>3,\*\*\*\*\*</sup>, A. Li<sup>4</sup>, F. Si<sup>4</sup>, J. Xu<sup>4</sup>, P-H. Xie<sup>4</sup>, W- Q. Liu<sup>4</sup>,**  
7 **A. Dzhola<sup>5</sup>, O. Postylyakov<sup>5</sup>, V. Ivanov<sup>5,\*\*\*\*\*</sup>, E. Grechko<sup>5</sup>, S. Terpugova<sup>6</sup>, and M.**  
8 **Panchenko<sup>6</sup>**

9 <sup>1</sup>Research Institute for Global Change, Japan Agency for Marine-Earth Science and  
10 Technology, Yokohama 2360001, Japan

11 <sup>2</sup>Nagoya University, Nagoya 4648601, Japan

12 <sup>3</sup>Gwangju Institute of Science and Technology (GIST), Gwangju 500712, Korea

13 <sup>4</sup>Anhui Institute of Optics and Fine Mechanics, Chinese Academy of Sciences, Hefei 230031,  
14 China

15 <sup>5</sup>A. M. Obukhov Institute of Atmospheric Physics, Russian Academy of Sciences, Moscow  
16 119017, Russia

17 <sup>6</sup> V. E. Zuev Institute of Atmospheric Optics, Siberian Branch of the Russian Academy of  
18 Sciences, Tomsk 634021, Russia

19 \* now at: Chiba University, Chiba 2638522, Japan

20 \*\* now at: Fukuoka University, Fukuoka 8140180, Japan

21 \*\*\* now at: Tohoku University, Sendai 9808578, Japan

22 \*\*\*\* now at: Asia Center for Air Pollution Research, Niigata 9502144, Japan

23 \*\*\*\*\* now at: Pukyong National University, Pusan 608737, Korea

24 \*\*\*\*\* now at: National Ozone Monitoring Research and Educational Center of Belarusian  
25 State University (NOMREC BSU), Minsk 220064, Belarus

26 Correspondence to: Y. Kanaya (yugo@jamstec.go.jp)

27 **Abstract.** We conducted long-term network observations using standardized Multi-Axis  
28 Differential optical absorption spectroscopy (MAX-DOAS) instruments in Russia and ASia  
29 (MADRAS) from 2007 onwards and made the first synthetic data analysis. At seven locations  
30 (Cape Hedo, Fukue, and Yokosuka in Japan, Hefei in China, Gwangju in Korea, and Tomsk  
31 and Zvenigorod in Russia) with different levels of pollution, we obtained 80,927 retrievals of  
32 tropospheric NO<sub>2</sub> vertical column density (TropoNO<sub>2</sub>VCD) and aerosol optical depth (AOD).  
33 In the technique, the optimal estimation of the TropoNO<sub>2</sub>VCD and its profile was performed  
34 using aerosol information derived from O<sub>4</sub> absorbances simultaneously observed at 460–490  
35 nm. This large data set was used to analyze NO<sub>2</sub> climatology systematically, including  
36 temporal variations from the seasonal to the diurnal scale. The results were compared with  
37 Ozone Monitoring Instrument (OMI) satellite observations and global model simulations.  
38 Two NO<sub>2</sub> retrievals of OMI satellite data (NASA ver. 2.1 and Dutch OMI NO<sub>2</sub> (DOMINO)  
39 ver. 2.0) generally showed close correlations with those derived from MAX-DOAS  
40 observations, but had low biases up to ~50%. The bias was distinct when NO<sub>2</sub> was abundantly  
41 present near the surface and when the AOD was high, suggesting a possibility of incomplete  
42 accounting of NO<sub>2</sub> near the surface under relatively high aerosol conditions for the satellite  
43 observations. Except for constant biases, the satellite observations showed nearly perfect  
44 seasonal agreement with MAX-DOAS observations, suggesting that the analysis of seasonal  
45 features of the satellite data were robust. Weekend reduction in the TropoNO<sub>2</sub>VCD found at  
46 Yokosuka and Gwangju was absent at Hefei, implying that the major sources had different  
47 weekly variation patterns. While the TropoNO<sub>2</sub>VCD generally decreased during the midday  
48 hours, it exceptionally increased at urban/suburban locations (Yokosuka, Gwangju, and Hefei)  
49 during winter. A global chemical transport model, MIROC-ESM-CHEM, was validated for  
50 the first time with respect to background NO<sub>2</sub> column densities during summer at Cape Hedo  
51 and Fukue in the clean marine atmosphere.

52

## 53 **1 Introduction**

54 Nitrogen oxides ( $\text{NO}_x$ ), i.e., NO and  $\text{NO}_2$ , are key chemical species in driving tropospheric  
55 photochemistry, and they participate in the mechanisms used to explain local to global air  
56 pollution. They are originally emitted or produced from natural (soil and lightning) and  
57 anthropogenic sources, and are strongly involved in the chain reactions forming tropospheric  
58 ozone ( $\text{O}_3$ ). The reaction of NO with peroxy radicals ( $\text{HO}_2$  and organic peroxy radicals,  $\text{RO}_2$ )  
59 produces  $\text{NO}_2$ , resulting in net production of  $\text{O}_3$  via subsequent photolysis of  $\text{NO}_2$ . This  
60 reaction simultaneously recycles OH radicals, which determine the atmospheric oxidative  
61 capacity, and this sustains the concentration levels of peroxy radicals. Under heavily polluted  
62 conditions,  $\text{NO}_2$  provides a major pathway for loss of OH, nonlinearly controlling the  
63 oxidative capacity. The deposition of nitric acid, produced from the reaction of  $\text{OH} + \text{NO}_2$ ,  
64 and of nitrate aerosols, normally formed by gas-to-particle partition of nitric acid, on the  
65 Earth's surface fertilizes terrestrial and marine ecosystems (Duce et al., 2008), as well as  
66 causing acidification. Knowledge of global and regional distributions of  $\text{NO}_2$ , their temporal  
67 variations, and the underlying mechanisms therefore provides a firm basis for investigations  
68 of multi-scale air pollution and the nitrogen cycle.

69 Recent orbiting satellite sensors have enabled monitoring of the tropospheric  $\text{NO}_2$  vertical  
70 column density (Tropo $\text{NO}_2$ VCD) from the regional to the global scale (e.g., Burrows et al.,  
71 1999). Past studies have shown that large spatial inhomogeneity, strong seasonal variations,  
72 and long-term trends are present (e.g., Richter et al., 2005; Boesma et al., 2007; Martin et al.,  
73 2006; van der A et al., 2008). In Asia, particularly Central East China ( $110\text{--}122^\circ \text{E}$ ,  $30\text{--}40^\circ \text{N}$ ),  
74 the highest Tropo $\text{NO}_2$ VCD values in the world have been recorded in recent years. Compared  
75 with the aerosol optical depth (AOD), another observable parameter from satellite sensors, for  
76 which various types of ground-based long-term monitoring networks such as AERONET  
77 (Aerosol RObotic NETwork, Holben et al., 2001), SKYNET (<http://atmos.cr.chiba-u.ac.jp/>),  
78 and light detection and ranging (lidar) networks can provide a firm basis for validation,

79 TropoNO<sub>2</sub>VCD has been evaluated with independent observations relatively infrequently. It  
80 is strategically important to certify satellite observations through comparisons with qualified  
81 observations regarded as ground truth; the verified spatial distributions or temporal variations  
82 are then used for further analysis.

83 In the past, aircraft-based in situ observations (Bucsela et al., 2008; Celarier et al., 2008),  
84 ground-based direct-sun Brewer measurements (Wenig et al., 2008), zenith DOAS  
85 (differential optical absorption spectroscopy) (Chen et al., 2009), lidar systems (Hains et al.,  
86 2010), urban air quality monitoring networks (Boersma et al., 2008), and combinations with  
87 model simulations (Lamsal et al., 2010) have been used for validation of satellite-based  
88 observations of tropospheric NO<sub>2</sub>. Multi-axis DOAS (MAX-DOAS) observations (Hönninger  
89 et al., 2004; Wittrock et al., 2004; Sinreich et al., 2005) have also been proven to provide  
90 suitable columnar data for validation of satellite observations. In the past, MAX-DOAS  
91 observations over relatively short periods have been used for the validation of satellite-based  
92 observations of tropospheric NO<sub>2</sub> (e.g., Heue et al., 2005, Brinksma et al., 2008, Celarier et al.,  
93 2008, Irie et al., 2008a, 2009a; Hains et al., 2010; Shaiganfar et al., 2011; Peters et al., 2012).  
94 For more systematic validation, a long-term ground-based monitoring network for NO<sub>2</sub> is  
95 highly desirable.

96 So far, several MAX-DOAS network observations have been reported. Two of these,  
97 established at an early stage, are the BREDOM (Bremian DOAS network for atmospheric  
98 measurements) network, including Bremen, Ny-Ålesund, Nairobi, Mérida, and Heraklion  
99 (e.g., Wittrock et al., 2004), and a network maintained by the Belgian Institute for Space  
100 Aeronomy (BIRA-IASB) (<http://uv-vis.aeronomie.be/groundbased/>), including Harestua,  
101 Jungfraujoch, Observatoire de Haute-Provence (OHP), Reunion Island, Beijing, and Uccle  
102 (e.g., Clémer et al., 2010). At these sites, high-quality spectroscopy is performed using  
103 high-grade spectrometers and charged-couple device (CCD) detectors, enabling retrievals of  
104 weak absorbers (e.g., BrO) in the troposphere and stratosphere. Valks et al. (2011) used

105 MAX-DOAS observations of TropoNO<sub>2</sub>VCD at OHP for 4 years to validate Global Ozone  
106 Monitoring Experiment-2 (GOME-2) satellite observations. Hendrick et al. (2013) studied  
107 temporal variations in NO<sub>2</sub> and HONO derived from MAX-DOAS observations for 4 years in  
108 and near Beijing.

109 As a Global Earth Observation System of Systems (GEOSS)-related project funded by the  
110 Japanese government during FY2006–2010, we established a long-term NO<sub>2</sub>-monitoring  
111 network based on MAX-DOAS over Russia and Asia (MADRAS). This paper provides an  
112 overview of these network observations. Our strategy is to use a relatively low-cost miniature  
113 spectrometer to obtain spectra of compromised, but still sufficient, quality. A similar approach  
114 was used for a network for monitoring volcano plumes (Galle et al., 2010). Recently, the Max  
115 Planck Institute reported long-term observations of NO<sub>2</sub> in Beijing using a low-cost  
116 MAX-DOAS instrument and comparisons of the data with satellite observations (e.g., Ma et  
117 al., 2013). Heidelberg University (Ulrich Platt, personal communication, 2011) operates about  
118 10 instruments, and the Anhui Institute of Optics and Fine Mechanics (AIOFM) runs more  
119 than 10 instruments within China (Wenqing Liu, personal communication, 2011), using a  
120 similar concept.

121 A major purpose of our network observations is to retrieve TropoNO<sub>2</sub>VCDs (and their  
122 vertical profiles) in the daytime to validate satellite observations at several key locations with  
123 different levels of air pollution, i.e., at Yokosuka, Cape Hedo, and Fukue (Japan), Gwangju  
124 (Korea), Hefei (China), and Zvenigorod and Tomsk (Russia). In addition, we aim to observe  
125 diurnal variations and vertical distributions of NO<sub>2</sub>, beyond the capabilities of current satellite  
126 sensors on sun-synchronous orbits with fixed local time observations. We also aim to validate  
127 tropospheric chemical transport model simulations using the long-term record.

128 In this paper, we describe instrumental aspects of the network observations, features of  
129 temporal variations in the retrieved TropoNO<sub>2</sub>VCD data during 2007–2012 (for 3 to more  
130 than 5 years of observations for each site), and comparisons with Ozone Monitoring

131 Instrument (OMI) satellite observations and global model simulations. The instruments used  
132 at the individual sites were standardized so that the basic optical components used were the  
133 same. The obtained spectra were processed centrally to maintain homogeneous data quality  
134 over the sites. Temporal variations from diurnal, weekly, seasonal, to multi-year scales were  
135 investigated, and compared with satellite observations wherever possible.

136

## 137 **2 Experimental**

### 138 **2.1 Instrumentation**

139 The MAX-DOAS instruments deployed at our network sites consisted of a light-receiving  
140 part and a miniature spectrometer connected by a bundle optical fiber cable (Fig. 1). The  
141 spectrometers used were USB4000 (Ocean Optics, Dunedin, FL, USA) equipped with a linear  
142 array of CCD detectors with 3648 pixels (TCD1304AP; Toshiba, Tokyo, Japan), except for  
143 the #1 instrument at Fukue, which was used for only 2 months (see Table 1), where another  
144 miniature spectrometer (BTC111; B&W TEK Inc., Newark, DE, USA) was used. The  
145 light-receiving part incorporated a flat rectangular mirror, with a 45° incidence angle, located  
146 in a weather-shielding quartz tube cap, and a telescope with a single plano-convex quartz lens  
147 of diameter 25 mm and a focal length of 40 mm. The telescope was coupled with an optical  
148 bundle fiber cable (length 1 m or 5 m) via an SMA (subminiature version A) connector, which  
149 consisted of seven cores (each with a diameter of 100 μm and a numerical aperture of 0.22).  
150 The cores formed a circle at the telescope side end and were aligned vertically at the exit, to  
151 fit to the slit shape of the spectrometer. The telescope restricted the field of view angle to less  
152 than 1°. The field of view angle was tested by introducing light into the fiber retrospectively  
153 from the exit side, and the divergence of the light after exiting the telescope was evaluated.

154 The rectangular mirror was rotated every 5 min to introduce scattered sunlight from the sky,  
155 with sequential elevation angles of 3, 5, 10, 20, 30, and 90°, to the spectrometer through the  
156 telescope and the fiber bundle. One cycle of observations at six elevation angles (with

157 integration for 5 min for each) took 30 min. The cycle was repeated on a 24-h basis. The  
158 spectrometer integration time was fixed at a value between 100 and 400 ms during the day  
159 and night. The integration time changed seasonally so that the maximum signal level reached  
160 the middle range (between 20,000 and 40,000) of the full dynamic range of the 16-bit A/D  
161 converter ( $2^{16} = 65,536$ ). A spectrum with a customized integration time was averaged over  
162 250–600 integration times so that a single average spectrum was recorded every minute.

163 The USB4000 spectrometers used a standard grating (#5, a holographic grating for UV,  
164 with a groove density of 1200). The linear array CCD detector used the manufacturer's  
165 upgraded quartz window with UV transmittance and a cylindrical lens to enhance the  
166 efficiency. The slit width was generally 25  $\mu\text{m}$ , except for the instrument installed at Cape  
167 Hedo, which had a slit width of 10  $\mu\text{m}$ . The spectrometers were customized so that a  
168 wavelength range from 230 to 560 nm was covered and a wavelength resolution below 0.7 nm  
169 in full-width at half-maximum (FWHM) was attained at the 407.783-nm mercury line. The  
170 resulting wavelength resolution in the 460–490 nm range, used for the analysis of  $\text{NO}_2$  and  $\text{O}_4$   
171 in this study, was observed to be between 0.4 and 0.7 nm. The spectrometer was further  
172 customized to improve coupling to the fiber cable: a key lock, normally used to reproduce the  
173 angular position of the linearly aligned fiber cores at the exit of the bundle cable (within the  
174 SMA connector) with respect to the slit vertically oriented at the spectrometer, was removed  
175 and the connection was manually optimized in the rotational direction. The distance from the  
176 fiber end to the spectrometer slit was simultaneously optimized by inserting thin nylon  
177 spacers into the bottom space of the ferrule of the SMA connector at the exit end of the fiber.  
178 Thus, in addition to wavelength resolution, the spectral symmetry (determining the slit  
179 function shape) was optimized at a mercury line (407.783 nm) for each instrument before  
180 installation. The original distance between the fiber end and the slit determined by the  
181 manufacturer was often too short to optimize the spectral symmetry, although the signal  
182 intensity was higher there than that at our optimized position.

183 Single-notch filters at 405, 442, 488, and 355 nm (NF03-405E-25, NF01-442U-25,  
184 NF03-488E-25; Semrock Inc., Rochester, NY, USA) with a blocking optical depth (OD) > 6  
185 and FWHM in the range of 9–14 nm, and a 355-nm notch-filter (Edmund Optics, Barrington,  
186 NJ, USA) with a blocking OD > 4 and FWHM of 18 nm, were used for stray-light  
187 characterization of the instrument. For typical daylight conditions, the stray light levels were  
188 estimated to be only 0.6–1.0% of the daylight signal levels at each wavelength.

189 The elevation angles need to be absolutely accurate. The base plate of the light-receiving  
190 unit, to which the central axis of the telescope was parallel, was first set to be horizontal,  
191 using a horizontal level embedded in the base plate (Fig. 2). Subsequently, the angular  
192 position of the reflecting mirror at elevation angle = 0° was carefully adjusted. A stepping  
193 motor (with an angle step of 0.038°), used for controlling the mirror angle, was equipped with  
194 an optical angular position sensor, with which the zero position was first roughly determined.  
195 Then, an additional offset angle (at a resolution of 0.1°) with respect to the sensor position  
196 was precisely adjusted until the reflecting mirror became fully horizontal. The offset angle  
197 thus determined was registered in the initial file of the software for the mirror rotation and  
198 was activated all the time. In this procedure, we used a second horizontal level (Fig. 2)  
199 embedded in a plate holding the reflecting mirror at a perpendicular angle. The level was  
200 easily seen from the top of the instrument through the quartz cap, facilitating setup in the field.  
201 All the elevation angles used for the observations were determined in this way relative to the  
202 zero position initially set at installation. The long-term drift (over more than 1 year) of the  
203 zero position was typically less than 0.2°.

204 A laptop computer was used to control the mirror rotation and to collect all the spectra and  
205 house-keeping information (e.g., temperature control). A small fan was present beneath the  
206 quartz tube cap to avoid sedimentation of large aerosol particles on the surface of the cap, to  
207 remove small water droplets/snowflakes, and to reduce the possibility of small animals (e.g.,  
208 spiders) interfering with the observations.



## 209 **2.2 Observation sites**

210 The instruments were deployed at seven locations (Figs. 3 and 4, Table 1): at Cape Hedo,  
211 Okinawa Island, southwest of Japan, in March 2007, at Yokosuka, Japan in April 2007, at  
212 Gwangju, Korea in February 2008, at Hefei, Anhui Province, China in March 2008, at  
213 Zvenigorod, Russia in October 2008, at Tomsk, Russia in January 2009, and at Fukue Island,  
214 Nagasaki Prefecture, west of Japan in February 2009. The geographic coordinates, altitudes,  
215 and the azimuth angles of the line of sight for each observation site are listed in Table 1. The  
216 Yokosuka site (about 30 km south of Tokyo) is located within an industrialized area that  
217 extends in the north–south direction along Tokyo Bay in the Kanto Plain. Cape Hedo is a  
218 remote site, located in the northern-most part of subtropical Okinawa Island (Takami et al.,  
219 2007; Kanaya et al., 2001), and is distant from major cities (40 km from Nago, population  
220 60,000 and 100 km from Naha, population 320,000). For these two sites, five-fold optical  
221 axes were prepared for simultaneous observations at different elevation angles during  
222 intensive campaign periods. Under normal long-term operation, however, only a single  
223 telescope was used and the elevation angles were sequentially scanned. Gwangju site at the  
224 Gwangju Institute of Science and Technology is 8 km north-northwest of the Gwangju city  
225 center (population 1.4 million). The Hefei site is in the campus of AIOFM, about 10 km  
226 northwest of the Hefei city center (population 4.4 million). The Gwangju and Hefei sites are  
227 regarded as suburban sites. The Zvenigorod Research Station, affiliated to the Institute of  
228 Atmospheric Physics, Russian Academy of Sciences (Yurganov et al., 2010), is located in a  
229 rural area ~50 km west of Moscow, whose population is ~10.5 million. The observatory is  
230 registered as a Network Detection of Atmospheric Composition Change site with respect to  
231 stratospheric NO<sub>2</sub> observations. The observations at Tomsk took place in the campus of the  
232 Institute of Atmospheric Optics, Siberian Branch of the Russian Academy of Sciences. The  
233 site is ~5 km east of the Tomsk city center, whose population is 520,000. For the two  
234 instruments located in Russia, the heat insulation was strengthened to tolerate low ambient

235 temperatures during winter (between  $-20$  and  $-40$  °C). The data from Tomsk are still being  
236 evaluated, and will not be used in the following discussions. The Fukue site is remote, away  
237 from major cities (e.g., 100 km from Nagasaki, population 440,000). The differences of the  
238 local time (LT) from UTC are +9 h for Cape Hedo, Yokosuka, Fukue and Gwangju, +8 h for  
239 Hefei, and +4 h for Zvenigorod.

240 At each site, the light-receiving unit of the MAX-DOAS instrument was located on the  
241 rooftop of single to five-story building. Three types of deployment layout were used with  
242 respect to the spectrometer (type A, B, and C, see Table 1). For type A and B, the spectrometer  
243 was located indoors in a customized thermoelectrically controlled refrigerator (type A) or in a  
244 temperature stabilized case (type B). The controlled temperature was 20 or 25 °C for type A  
245 and 40 °C for type B for all seasons. For type C, the spectrometer was located outdoors in a  
246 light-receiving unit and its temperature was controlled to seasonally-changing levels (25 or  
247 30 °C in winter and 35 or 45 °C in summer). The precise temperature stabilization within  
248  $\pm 0.2$  °C (using KT4; Panasonic, Kadoma, Japan) on a 24-h basis was important for the  
249 purpose of subtracting the dark spectrum measured during the night from the daytime spectra.  
250 A large part of the pixel-to-pixel pattern variability in the dark spectrum was constant over  
251 time, as long as the temperature was constant. For example, in the case of 38 °C, the  
252 pixel-to-pixel variability was as much as 96 digits as a standard deviation ( $1\sigma$ ), for a spectrum  
253 obtained with an integration time of 100 ms averaged 600 times. However, after subtraction of  
254 the averaged dark “pattern” spectrum, recorded during the night-time, the random noise  
255 (pixel-to-pixel) was as small as 2–3.5. A signal-to-noise ratio of the order of  $10^4$  was therefore  
256 expected, which was typically required to analyze weak absorptions ( $<0.1\%$ ) quantitatively.  
257 Temperature stabilization was also important for keeping the wavelength shift constant over a  
258 long time period.

259

## 260 **2.3 Retrieval algorithms**

261 The recorded spectra were processed centrally so that the network observations produced data  
262 of homogeneous quality. The retrieval algorithm was similar to that used for JM1 (Irie et al.,  
263 2011), but (1) QDOAS software ver. 2.00 (<http://uv-vis.aeronomie.be/software/QDOAS/>, Fayt  
264 and Roozendael, 2012) was used for DOAS analysis, and (2) a newly coded Fortran program  
265 was used for subsequent conversion of the differential slant column densities ( $\Delta$ SCDs) to  
266 vertical quantities. The basic flow of the analysis was similar to that used previously (Irie et  
267 al., 2008a,b, 2009a). Briefly, the measured spectra of scattered sunlight in the range of  
268 460–490 nm at low elevation angles were analyzed, using the DOAS technique (Platt, 1994),  
269 to retrieve the  $\Delta$ SCDs of oxygen collision complexes ( $O_2-O_2$  or  $O_4$ ) and  $NO_2$  with respect to  
270 the reference spectrum obtained at the highest elevation angle ( $90^\circ$  or  $70^\circ$ ). A reference  
271 spectrum was derived by interpolating two spectra measured within 30 min before and after  
272 the off-axis measurement. The absorption by gaseous species, i.e.,  $O_4$ ,  $NO_2$ ,  $O_3$ , and  $H_2O$ , and  
273 the Ring effect were taken into account. The absorption cross-sections used were those  
274 reported by Herman et al. (<http://spectrolab.aeronomie.be/o2.htm>) for  $O_4$ , Vandaele et al.  
275 (1996) for  $NO_2$  at 298 K, Bogumil et al. (2003) for  $O_3$  at 223 K, and Rothman et al. (2003) for  
276  $H_2O$ . The cross-sections of  $O_4$  were increased by a factor of 1.25, following Cl mer et al.  
277 (2010). A polynomial degree of three was used to fit the continuum. Typical residuals of  
278 spectral fitting were in the range of  $(5-20) \times 10^{-4}$  for clear midday periods, but they increased  
279 in the early morning and late evening.

280 The  $O_4$   $\Delta$ SCD values were next converted to the AODs and vertical profiles of the aerosol  
281 extinction coefficients, using the optimal estimation method (OEM) developed by Rodgers  
282 (2000). The measurement vector consisted of five  $O_4$   $\Delta$ SCD values observed at low elevation  
283 angles. The state vector consisted of the AOD and three parameters ( $f_1$ ,  $f_2$ , and  $f_3$ ) determining  
284 the vertical profiles, with which the partial optical depths for the altitude ranges 0–1, 1–2, and  
285 2–3 km were expressed as  $f_1 \times AOD$ ,  $(1 - f_1) \times f_2 \times AOD$ , and  $(1 - f_1) \times (1 - f_2) \times f_3 \times AOD$ ,  
286 respectively (see Irie et al., 2008b). The a priori values and the errors in the AOD,  $f_1$ ,  $f_2$ , and  $f_3$

287 were chosen to be  $0.21 \pm 3.0$ ,  $0.60 \pm 0.05$ ,  $0.80 \pm 0.03$ , and  $0.80 \pm 0.03$ , respectively. A lookup  
288 table of box air mass factors ( $A_{\text{box}}$ ), which characterized the ratio of the partial slant to the  
289 vertical columns for a given layer, was created using a three-dimensional Monte Carlo  
290 radiative transfer model, MCARaTS (Iwabuchi, 2006).  $A_{\text{box}}$  calculations using MCARaTS  
291 have been validated through comparisons with other radiative transfer models (Wagner et al.,  
292 2007). An optimal aerosol (and  $A_{\text{box}}$ ) profile scenario that accounted for the  $\text{O}_4$   $\Delta\text{SCD}$  values  
293 measured at all elevation angles was determined.

294 Using the  $A_{\text{box}}$  profiles and an iterative inversion method similar to that used for aerosol  
295 retrieval, a set of  $\text{NO}_2$   $\Delta\text{SCD}$  values for low elevation angles (as the measurement vector) was  
296 then converted to a tropospheric VCD and a vertical profile of  $\text{NO}_2$  using an OEM. The state  
297 vector included Tropo $\text{NO}_2$ VCD, and the partial fraction parameters  $v_1$ ,  $v_2$ , and  $v_3$ , with which  
298 the partial  $\text{NO}_2$  VCDs in the altitude ranges 0–1, 1–2, and 2–3 km were expressed as  
299 Tropo $\text{NO}_2$ VCD  $\times v_1$ , Tropo $\text{NO}_2$ VCD  $\times (1 - v_1) \times v_2$ , and Tropo $\text{NO}_2$ VCD  $\times (1 - v_1) \times (1 -$   
300  $v_2) \times v_3$ , respectively. The a priori values for Tropo $\text{NO}_2$ VCD,  $v_1$ ,  $v_2$ , and  $v_3$  were selected to be  
301 20% of the largest  $\Delta\text{SCD}$  values for  $\text{NO}_2$ ,  $0.60 \pm 0.05$ ,  $0.80 \pm 0.03$ , and  $0.80 \pm 0.03$ ,  
302 respectively. The  $\text{NO}_2$   $\Delta\text{SCD}$  determinations using an instrument of the same design were  
303 validated during the CINDI 2009 (Cabauw Intercomparison Campaign of Nitrogen Dioxide  
304 measuring Instruments) campaign performed at Cabauw, the Netherlands, during June–July  
305 2009 (Roscoe et al., 2010; Piters et al., 2012). The compatibility of the Tropo $\text{NO}_2$ VCD data  
306 with those derived using the JM1 algorithm (Irie et al., 2011) was also confirmed.

307 Takashima et al. (2009) established an original cloud-screening method for studying  
308 aerosols at Cape Hedo using a combination of the MAX-DOAS color index (defined as the  
309 ratio of the intensities at 500 and 380 nm) and the relative humidity, derived from  $\text{H}_2\text{O}$   
310 retrieved from the MAX-DOAS analysis. However, for the retrieval of  $\text{NO}_2$ , which is the  
311 main target of this study, critical cloud screening using the color index was not applied,  
312 because the  $\text{NO}_2$  state would be retrieved properly as long as the optical path length was

313 determined correctly. It should also be noted that even without such screening using the color  
314 index, a large fraction of cloudy cases was eliminated in advance, as the observed O<sub>4</sub> ΔSCD  
315 values at five elevation angles were irregularly distributed and were not well fitted. See the  
316 supplementary material for details of cloud screening using the color index applied for the  
317 evaluation of the retrieved aerosol quantities.

318 Error estimation methodologies have been reported for random and systematic uncertainties  
319 in aerosol retrievals (Irie et al., 2008a; Takashima et al., 2009). The overall uncertainty in the  
320 AOD was estimated from our past comparisons with existing methods (sky radiometer and  
321 Mie lidar) to be 30%. The method used to calculate random and systematic uncertainties in  
322 TropoNO<sub>2</sub>VCD has been described elsewhere (Irie et al., 2009a, 2011). The random  
323 uncertainty was estimated to be 10%, based on the residuals in the ΔSCD fitting. The  
324 systematic error was estimated to be 14%, to which the uncertainties in the AOD and in the  
325 A<sub>box</sub> contributed by similar degree. The combined total uncertainty was typically 17%.  
326 Takashima et al. (2011, 2012) reported that similar instruments had detection limits for NO<sub>2</sub>  
327 mixing ratios of <0.2 ppb at an altitude of 0–1 km, corresponding to a minimum detectable  
328 TropoNO<sub>2</sub>VCD of  $<5 \times 10^{14}$  molecules cm<sup>-2</sup>.

329 Figure 5 demonstrates the performance of our retrievals for selected morning hours  
330 [0800–0900 (8 h) or 0900–1000 (9 h) LT], and afternoon hours [1500–1600 (15 h) or  
331 1600–1700 (16 h) LT] in June at three locations (Zvenigorod, Hefei, and Yokosuka). The O<sub>4</sub>  
332 ΔSCD values (Figs. 5a–c) showed negative dependences on the elevation angles, and they  
333 were well fitted using the OEM. The low O<sub>4</sub> ΔSCD values at Hefei at all elevation angles (Fig.  
334 5b) were explained by the presence of dense aerosols. The O<sub>4</sub> ΔSCD values in the afternoon  
335 were higher at Hefei (Fig. 5b) and Yokosuka (Fig. 5c), and lower at Zvenigorod (Fig. 5a), than  
336 those in the morning; this was mainly explained by differences among the relative azimuth  
337 angles of observation. The retrieved AOD values were similar for the morning and afternoon  
338 at all the sites. The NO<sub>2</sub> ΔSCD values were higher in the morning than in the afternoon in all

339 cases (Figs. 5d–f), because NO<sub>2</sub> was more abundant in the morning. At Zvenigorod and Hefei,  
340 the NO<sub>2</sub> ΔSCD values showed a stronger dependence on the elevation angle in the morning  
341 than in the afternoon, resulting in steeper vertical profiles (and higher  $\nu_1$  values) in the  
342 morning (Figs. 5g and h). At Yokosuka, the dependence of the NO<sub>2</sub> ΔSCD values on elevation  
343 angle did not greatly change from the morning to the afternoon, and therefore the  $\nu_1$  values  
344 and the vertical profiles of NO<sub>2</sub> were almost unchanged diurnally. This could be explained by  
345 continuous NO<sub>x</sub> emissions from nearby sources at Yokosuka, sustaining a relatively steep  
346 vertical gradient at all times. In contrast, the less steep vertical gradients in NO<sub>2</sub> up to 2 km at  
347 Zvenigorod and Hefei in the afternoon could be explained by the fact that nearby sources  
348 were less important, and that the continental boundary layer height became thicker in the  
349 afternoon during summer. The degrees of freedom of the signal typically exceeded two during  
350 the daytime periods between the morning and afternoon hours studied here.

351 The final products of our retrieval were TropoNO<sub>2</sub>VCDs, AODs, vertical profiles of NO<sub>2</sub>  
352 and extinction coefficients, with a resolution of 1 km (up to 3 km) at a time resolution of 30  
353 min during daytime. Careful quality control of the data was applied to remove cases with  
354 wrong mirror operations, power blackouts, shifts in the dark spectra as a result of changes in  
355 integration time and temperature settings, large residuals in the spectral fittings, malfunction  
356 in the temperature control, and saturated signal levels.

#### 357 **2.4 OMI satellite data products for comparison**

358 In this section OMI satellite data products of TropoNO<sub>2</sub>VCD, to be compared with our  
359 MAX-DOAS products in section 3.1, are summarized. The OMI is a UV/vis nadir viewing  
360 spectrometer on the National Aeronautics and Space Administration (NASA) Aura satellite on  
361 a sun synchronous orbit launched in 2004. An OMI pixel size is 13 × 24 km<sup>2</sup> or larger. We  
362 used two different products, i.e., one derived from the algorithm developed by the NASA and  
363 the other from the algorithm (Dutch OMI NO<sub>2</sub> (DOMINO)) developed by Koninklijk  
364 Nederlands Meteorologisch Instituut. The NASA data set was the ver. 2.1 release of the

365 gridded OMNO2d daily level 3 products (OMNO2d.003), with cloud screening at 30%, at a  
366 resolution of  $0.25^\circ \times 0.25^\circ$ , available from the NASA Giovanni website  
367 ([http://gdata1.sci.gsfc.nasa.gov/daac-bin/G3/gui.cgi?instance\\_id=omi](http://gdata1.sci.gsfc.nasa.gov/daac-bin/G3/gui.cgi?instance_id=omi); Bucselá et al., 2013).  
368 The latter data set was the monthly DOMINO ver. 2.0 collection 3, at a resolution of  $0.125^\circ \times$   
369  $0.125^\circ$ , available from the Tropospheric Emission Monitoring Internet Service (TEMIS)  
370 website ([http://www.temis.nl/airpollution/no2col/no2regioomimonth\\_col3.php](http://www.temis.nl/airpollution/no2col/no2regioomimonth_col3.php); Boersma et al.,  
371 2011). The data at the nearest grid were used for both products. For the DOMINO algorithm,  
372 the results at eight adjacent grids were included (gray lines in Fig. 7) in addition to the nearest  
373 grid, to represent the spatial inhomogeneity of  $\text{NO}_2$  over the range  $0.375^\circ \times 0.375^\circ$ .

374 The two algorithms subtract stratospheric  $\text{NO}_2$  component as simulated by a chemical  
375 transport model (DOMINO ver 2.0) or determined directly from satellite data (NASA ver. 2.1)  
376 from the total and then determine TropoNO2VCD using tropospheric air mass factors. For  
377 both satellite data products, air mass factors were computed as average of clear and cloudy  
378 conditions weighted by the cloud radiation fraction, and therein the aerosols are implicitly  
379 taken into account similarly to clouds (Boersma et al., 2011; Bucselá et al., 2013). They both  
380 adopt the vertical profile shapes of  $\text{NO}_2$  simulated by global chemical transport models at  
381 relatively coarse resolutions (TM4 at  $2^\circ \times 3^\circ$  for DOMINO and GMI at  $2^\circ \times 2.5^\circ$  for NASA)  
382 but with down to monthly time resolution. The uncertainty for individual retrievals of  
383 TropoNO2VCD was estimated to be  $1.0 \times 10^{15}$  molecules  $\text{cm}^{-2} + 25\%$  (Boersma et al., 2011),  
384 and on the order of  $10^{15}$  molecules  $\text{cm}^{-2}$  (Bucselá et al., 2013) for clear-sky conditions.  
385 Observational information content with respect to vertical profiles of  $\text{NO}_2$  and the amount of  
386 aerosols is less than the case of MAX-DOAS observations; advantages of MAX-DOAS are  
387 that 1) observations of  $\Delta\text{SCDs}$  of  $\text{NO}_2$  at multiple axes are available, 2) simultaneous  
388 determination of aerosols is enabled using  $\text{O}_4$  absorbance determined in the same axes, and 3)  
389 the determined aerosol quantities are explicitly taken into account in the  $\text{NO}_2$  retrievals,  
390 although data at fixed locations with the instruments are only available.

391

### 392 **3 Results and Discussion**

393 We focus on NO<sub>2</sub> in this paper, so evaluation of our AOD results is included in the  
394 supplementary material. The NO<sub>2</sub> data obtained at Yokosuka and Hedo have been partly used  
395 for validation of TropoNO<sub>2</sub>VCD derived from OMI and other satellite sensors (Irie et al.,  
396 2009a, 2012), comparisons with ship-based observations (Takashima et al., 2012), and for  
397 analysis of transport from the Asian continent (Takashima et al., 2011). In this paper,  
398 independently of previous papers, we focus on features of temporal variations at multiple time  
399 scales (e.g., diurnal, weekly, and seasonal variations) of TropoNO<sub>2</sub>VCD. Comparisons with  
400 satellite-based TropoNO<sub>2</sub>VCD are also made wherever possible. Finally, we include  
401 comparisons with the simulation results from a global chemical transport model at Cape Hedo  
402 and Fukue.

403

#### 404 **3.1 Variations on seasonal or longer scales: comparisons with OMI**

405 Figure 6 shows the full records of the TropoNO<sub>2</sub>VCDs for all the sites, including data during  
406 the whole daytime period, until December 2012. Table 1 summarizes the number of  
407 successful NO<sub>2</sub> retrievals for each site; in total, 80,927 data are included in the analysis in this  
408 paper. They are subsets of 180,654 data for which  $\Delta$ SCDs of NO<sub>2</sub> and O<sub>4</sub> for all elevation  
409 angles were successfully determined and 90,644 data for which aerosol retrievals were  
410 successful, after careful data screening with respect to the instrumental conditions. The VCD  
411 levels were highest (at around  $10^{16}$ – $10^{17}$  molecules cm<sup>-2</sup>) at Yokosuka, an urban site, and  
412 lowest (at around  $3 \times 10^{14}$  to  $5 \times 10^{15}$  molecules cm<sup>-2</sup>) at Cape Hedo, a remote site; the VCD  
413 levels from other sites (Hefei, Gwangju, Zvenigorod, and Fukue, in descending order) were  
414 between these. Altogether, our TropoNO<sub>2</sub>VCD data ranged over more than two orders of  
415 magnitudes. The wide dynamic range and its full coverage were advantageous for the  
416 validation of satellite data, as shown later.



417 Figure 7 shows time series of monthly averaged MAX-DOAS observations (during  
418 1300–1400 LT, except for 1500–1600 LT at Zvenigorod, matching satellite overpass timings)  
419 and satellite observations of TropoNO<sub>2</sub>VCD from the OMI sensor. As mentioned in Section  
420 2.4, two different products with different algorithms (NASA and DOMINO) were used.

421 At Cape Hedo and Fukue, where the local sources were negligible and thus the  
422 observations were ideally representative over the grids described above (or over the footprint  
423 size of the satellite observations, i.e.,  $24 \times 13 \text{ km}^2$  or larger), the concentration levels and  
424 variation patterns were in relatively good agreement (Fig. 7a and b). At the two sites, the  
425 previous data product from NASA (ver. 1) always yielded significantly higher levels (Fig. 7a  
426 and b). After revision of the data set, disagreements with the MAX-DOAS observations  
427 disappeared and the agreement improved. For relatively low ranges of TropoNO<sub>2</sub>VCD ( $< \sim 3 \times$   
428  $10^{15} \text{ molecules cm}^{-2}$ ), precise subtraction of the stratospheric component of NO<sub>2</sub> is important  
429 for satellite observations; this might have been the source of differences, although full  
430 identification of the cause is beyond the scope of this paper.

431 The monthly variation pattern at Zvenigorod (Fig. 7f), in the middle range, i.e.,  $\sim 10 \times 10^{15}$   
432  $\text{molecules cm}^{-2}$ , is very well reproduced by the satellite observations. The satellite data  
433 capture the decreasing and increasing trends found using the MAX-DOAS observations from  
434 April to October in 2011 and 2012, respectively.

435 In contrast, in polluted areas with TropoNO<sub>2</sub>VCD values normally exceeding  $10 \times 10^{15}$   
436  $\text{molecules cm}^{-2}$ , for example, at Yokosuka and Gwangju (Fig. 7c and d), the MAX-DOAS  
437 observations tended to be higher than both satellite-derived values. The spatial variability of  
438 the NO<sub>2</sub> values over the nine grids for the DOMINO data set was relatively small and did not  
439 extend to the average levels of the MAX-DOAS observations in winter at Yokosuka. This  
440 may indicate that spatial inhomogeneity alone cannot explain the difference between the  
441 MAX-DOAS and satellite observations, although the inhomogeneity at scales smaller than  
442  $0.125^\circ$  could be responsible for the differences. It should be noted that the MAX-DOAS

443 observations are representative over a distance of about 2–10 km on the line of sight.

444 Figures 8a and b show summary scatterplots of the monthly averaged TropoNO<sub>2</sub>VCD  
445 values from observations by MAX-DOAS and those by OMI with two algorithms, DOMINO  
446 ver. 2.0 and NASA ver. 2.1. The correlations were very tight for both cases, with  $R^2$  values  
447 exceeding 0.84, suggesting that the two satellite-derived products captured monthly variations  
448 quite well. However, the slopes were  $\sim 0.5$  for both cases, suggesting that the satellite  
449 observations tended to give lower values than the MAX-DOAS observations did, and were  
450 strongly influenced by the data in the high range. The deviation from unity cannot be  
451 explained by the combined uncertainties in the satellite observations ( $\sim 25\%$ , Boersma et al.,  
452 2011) and MAX-DOAS.

453 When we limited the data to months where 1) more than 50% of the days of satellite  
454 observations were overlapped with MAX-DOAS observations and vice versa, and 2)  
455 coincident observations were made on 5 or more days, the  $R^2$  value became even larger ( $R^2 =$   
456 0.88), but the slope remained at around 0.5. When the observation sites were grouped into two  
457 types, i.e., urban/suburban (Yokosuka, Gwangju, and Hefei) and rural/remote (Zvenigorod,  
458 Fukue, and Cape Hedo), the slopes were almost unchanged (0.54) for the urban/suburban case,  
459 whereas those for the rural/remote type increased to 0.78 and 0.63 with  $R^2$  values of 0.74 and  
460 0.65, with respect to DOMINO and NASA products, respectively (Figs 8c and d). This  
461 suggested the possibility that the observations at the three sites categorized as urban/suburban  
462 type did not represent the grids, and the spatial inhomogeneity could partly explain the larger  
463 departure of the slope value from unity.

464 This magnitude relationship was the opposite to those found in previous validation studies,  
465 which suggested the DOMINO products (ver. 1.02) had a high bias, i.e., 0–40% (Hains et al.,  
466 2010; Huijnen et al., 2010; Lamsal et al., 2010; Zhou et al., 2009), as summarized by  
467 Boersma et al. (2011). The revisions from DOMINO ver. 1.02 to the current version (ver. 2.0)  
468 were too small at the three urban/suburban sites (i.e., Yokosuka, Gwangju, and Hefei) to

469 explain the different results. However, recent studies suggested low biases, 26–38% and  
470 ~50%, in Beijing and in Delhi and its surroundings, respectively (Ma et al., 2013; Shaiganfar  
471 et al., 2011), in agreement with the magnitude relationship we found for the three  
472 urban/suburban sites.

473 Figure 9 shows the scatterplots between MAX-DOAS and OMI satellite observations at  
474 satellite pixel levels ( $n = 813$ , for six sites altogether) using more strict coincidence criteria  
475 (horizontal displacement  $<0.15^\circ$ , time difference  $<15$  min) and cloud screening (cloud  
476 fraction  $<10\%$ ). This also resulted in a similar underestimation of TropoNO<sub>2</sub>VCD for the  
477 satellite data; the slopes were 0.53 and 0.46, against DOMINO (ver. 2.0) and NASA (ver. 2.1),  
478 respectively. The slopes for the three cleaner sites were similar (0.55 and 0.42, respectively).  
479 This analysis indicated that a slope value lower than unity cannot be attributed to the poor  
480 overlap of the measurement days in each month or to the spatial inhomogeneity down to the  
481 scales of the footprint size of the satellite observations.

482 Another possibility would be that systematic underestimation by satellite observations  
483 arises from assumptions in the vertical profiles and aerosol treatment. Figure 10a shows that  
484 low OMI(NASA)/MAX-DOAS ratios (using a gridded data set for OMI) are associated with  
485 high AODs (as observed by MAX-DOAS); although the median ratio is near unity at low  
486 AODs ( $\sim 0.1$ ), it becomes lower ( $\sim 0.7$ ) with AODs as high as 1. In this study, only data with  
487 more than  $1 \times 10^{15}$  molecules  $\text{cm}^{-2}$  for both MAX-DOAS and satellite observations are used.  
488 This suggests the possibility that the satellite observations underestimate TropoNO<sub>2</sub>VCD  
489 when aerosols are densely present. This is less likely to be explained by overestimation by  
490 MAX-DOAS at high AODs, where larger observational information content regarding  
491 aerosols (multiple axis measurements of O<sub>4</sub>) were used in the derivation of  $A_{\text{box}}$  and  
492 TropoNO<sub>2</sub>VCD. All of the data ( $n = 1834$  from the six sites) were subdivided into two groups  
493 of equal size, based on AOD values (i.e., two groups with high and low AOD values) and a  
494 Welch's t-test was applied to test the statistical significance of the difference between the two

495 means. The results suggested that the OMI(NASA)/MAX-DOAS ratio was significantly lower  
496 for the group with higher AODs at the 95% confidence level. Similar tests for individual sites  
497 led to the same conclusion for Fukue, Zvenigorod, and Gwangju.

498 Figure 10b shows that the OMI(NASA)/MAX-DOAS ratio for TropoNO<sub>2</sub>VCD had a weak  
499 decreasing trend with the retrieved parameter  $v_1$ , the fraction of NO<sub>2</sub> present in the lowest 1  
500 km. The median values decreased from around unity to 0.67 as  $v_1$  increased from ~0.6 to 0.9.  
501 Welch's t-tests applied to two groups of data sorted by  $v_1$  values suggested that the ratio was  
502 significantly lower for the group with higher  $v_1$  values when using data from all six sites and  
503 when using data from Yokosuka and Hefei individually, at the 95% confidence level. This  
504 suggests that the underestimation occurs when NO<sub>2</sub> is mostly present near the surface. These  
505 analyses, in combination, imply that the lower values from the satellite could be partly caused  
506 by the assumptions made regarding the vertical profiles and aerosol treatment in the satellite  
507 data analysis. This may be important at clean sites, where the spatial inhomogeneity cannot be  
508 responsible for the difference. For both satellite data products, air mass factors were computed  
509 as average of clear and cloudy conditions weighted by the cloud radiation fraction, and therein  
510 the aerosols are implicitly taken into account similarly to clouds (Boersma et al., 2011;  
511 Bucsela et al., 2013). Considering that the variance of the ratio was only partly explained by  
512 AOD (Fig. 10a), one could argue that the effect of aerosols was almost successfully removed  
513 even in the current satellite data retrieval. However, a weak dependence of the ratio on AOD  
514 was still discernible, suggesting that the retrieval could be improved by an explicit treatment  
515 of the aerosols. Leitão et al. (2010) theoretically demonstrated that such underestimation by  
516 satellite observations could occur when the aerosol layer extends to relatively higher altitudes  
517 than NO<sub>2</sub>. Recently, Shaiganfar et al. (2011) and Ma et al. (2013) implied that the shielding  
518 effect of NO<sub>2</sub> by aerosols could be the cause of low biases in OMI observations over India  
519 and China. Lin et al. (2013) suggested that concentration of aerosols at the top of the  
520 boundary layer increased retrieved NO<sub>2</sub> by 8%.

521 From the above analyses of correlations and dependences on AOD and  $v_1$ , we conclude that  
522 the values of the OMI satellite data for TropoNO<sub>2</sub>VCD were lower than those from the  
523 network MAX-DOAS observations, and were possibly affected by the presence of aerosols,  
524 the assumptions made regarding the vertical profile of NO<sub>2</sub>, and how representative the site is  
525 (for the urban/suburban cases).

526 Figure 11 shows the averaged seasonal variations in the MAX-DOAS and satellite-based  
527 observations. MAX-DOAS data recorded during 1300–1400 LT (1500–1600 LT for  
528 Zvenigorod), matching satellite overpass timings, were used. Here, the right-axis scales for  
529 the OMI-derived quantities were adjusted by factors of 1.23, 1.54, 1.76, 1.77, 1.71, and 1.07  
530 for Cape Hedo, Fukue, Yokosuka, Gwangju, Hefei, and Zvenigorod, respectively. At almost  
531 all sites except Zvenigorod, TropoNO<sub>2</sub>VCD had a clear summer minimum and winter  
532 maximum. This feature can be interpreted using a combination of 1) seasonal changes in NO<sub>x</sub>  
533 emissions, 2) efficient partitioning to NO via faster photolysis rates of NO<sub>2</sub> in summer, and 3)  
534 efficient oxidation of NO<sub>2</sub> by OH in summer. Van der A et al. (2008) suggested, based on their  
535 analysis of GOME and SCIAMACHY (SCanning Imaging Absorption spectroMeter for  
536 Atmospheric CartographY) satellite data that the wintertime maximum indicates the  
537 dominance of NO<sub>x</sub> sources from anthropogenic sectors (fossil fuel and biofuel combustion).  
538 Each of our observation sites had unique features in their seasonal patterns (Fig. 11), and the  
539 satellite data captured such detailed features quite well. For example, seasonal variations at  
540 Fukue Island and Hefei were relatively symmetric with respect to June/July. At Yokosuka and  
541 Gwangju, decreases in spring were slow, but increases in fall were relatively rapid. The  
542 wintertime peak occurred in December at Gwangju, whereas it appeared in January at Hefei.  
543 At Zvenigorod, low levels lasted for a short period during June–August, and the values in  
544 April and May, and in October, were larger. All these detailed features were quite well  
545 reproduced by the satellite observations.

546 Deviations of pixel-level OMI(NASA) TropoNO<sub>2</sub>VCD from monthly mean values

547 positively correlated with those for coinciding MAX-DOAS observations (Fig. 12, with  $R^2$   
548 values of 0.45) with a slope of 0.40, a similar value of those in Fig. 9. This suggested that the  
549 satellite observation successfully captured day-to-day variations in addition to the monthly  
550 variations, although the sensitivity was consistently small.

551 The observed features in the year-to-year variations were also well reproduced by the  
552 satellite observations (Fig. 7). For example, relatively high values in January 2011 at Cape  
553 Hedo, and those in December 2009 and January 2010 at Fukue were well captured.

554

### 555 **3.2 Diurnal and weekly variations**

556 Figure 13 shows the diurnal variations averaged for each month. Generally, daytime decreases  
557 were recorded, as a result of 1) stronger emissions in the early morning, 2) effective  
558 partitioning to NO in the daytime by  $\text{NO}_2$  photolysis, and 3) stronger oxidation of  $\text{NO}_2$  by OH,  
559 similar to the causes for the summer minima. At Cape Hedo, such a pattern of daytime  
560 decreases was clearly seen for all months (Fig. 13a). In contrast, at Yokosuka, Gwangju, and  
561 Hefei (Fig. 13c–e) in winter, daytime increases in Tropo $\text{NO}_2$ VCD were observed. The  
562 periods with daytime increases were November–February at Yokosuka, November–December  
563 at Gwangju, and December–January at Hefei, slightly different from site to site. This feature  
564 was interpreted as 1) accumulation of pollutants overriding the loss rates and/or 2) importing  
565 of more polluted air masses in the afternoon period. Particularly at Yokosuka, located about  
566 30 km south of the Tokyo metropolitan area, the wintertime northerly wind tended to carry  
567 more polluted air masses from northern areas near Tokyo to the south, resulting in higher  $\text{NO}_2$   
568 concentrations in the afternoon. Similar daytime increases in Tropo $\text{NO}_2$ VCD during winter  
569 were reported in Greenbelt, Maryland, USA (Wenig et al., 2008) and in/near Beijing, China  
570 (Ma et al., 2013; Hendrik et al., 2013). Figure 14a shows that the diurnal variation patterns for  
571 the partial column of  $\text{NO}_2$  in the 0–1 km altitude range in four selected months, January, April,  
572 July, October at Yokosuka, are quite similar to those for  $\text{NO}_2$  measured at a nearby

573 air-quality-monitoring site (Nagahama site, about 4 km to the northwest). The NO<sub>2</sub>  
574 monitoring was performed using a chemiluminescence instrument equipped with a  
575 molybdenum converter, and thus was potentially influenced by other NO<sub>z</sub> species; in the  
576 urban locations near Tokyo, however, the influence was small (e.g., Kondo et al., 2008). In  
577 this study, we only compared the diurnal patterns. In the afternoons in January, the patterns  
578 were significantly different. The air mass on the line of sight of MAX-DOAS over Tokyo Bay  
579 could have been more influenced by the transport of polluted air masses from the Tokyo  
580 region or by ship emissions in the afternoon in winter.

581 Figure 15 shows the diurnal variations averaged separately for each day of the week.  
582 Apparent holidays for each country were re-categorized as Sundays. Although almost no  
583 weekend reductions were observed at remote locations (Cape Hedo and Fukue, Fig. 15a and  
584 b), the TropoNO<sub>2</sub>VCD values were clearly lower on Sundays at Yokosuka and Gwangju,  
585 because of the lower emissions from nearby sources, primarily as a result of less traffic (e.g.,  
586 diesel trucks). At a similar suburban site, i.e., Hefei, however, this weekly cycle was not  
587 observed (Fig. 15e). This different behavior suggests that the NO<sub>x</sub> emission rate from the  
588 major sector there does not follow a weekly cycle. It has been estimated from an Asian  
589 emission inventory for INTEX-B for 2006 that 24%, 58%, and 61% of NO<sub>x</sub> emission are from  
590 the transportation sector for China, Korea, and Japan, respectively (Zhang et al., 2009). The  
591 lower contribution from the transport sector for China probably causes this difference. The  
592 negligible weekly variation in China was consistent with the results of an earlier study using  
593 GOME data (Beirle et al., 2003). Similar results without weekend anomalies were found by  
594 Ma et al. (2013) for MAX-DOAS observations in Beijing.

595 Figure 14b shows that the average diurnal profiles of the partial vertical columns of NO<sub>2</sub> in  
596 the 0–1 km altitude range for weekdays, Saturdays, and Sundays at Yokosuka are in nearly  
597 perfect agreement with those for NO<sub>2</sub> monitoring at the Nagahama site. These analyses of  
598 diurnal and weekly behaviors of NO<sub>2</sub> help to refine the emission inventory of NO<sub>x</sub>. For the

599 Kanto area, including Yokosuka and Tokyo, NO<sub>x</sub> emissions on Sundays were estimated to be  
600 lower by 45% (Kannari et al., 2007) for the year 2000, which is roughly in agreement with  
601 our observations (37% reduction on Sundays for 0700–1600 LT). A more detailed comparison  
602 between observed and modeled NO<sub>2</sub> at Yokosuka is planned, to refine the emission  
603 inventories and to test the unique wintertime diurnal variation there.

604 Figure 16 compares the MAX-DOAS-derived reduction ratios for TropoNO<sub>2</sub>VCD at  
605 weekends (for Saturdays and Sundays separately) with respect to weekdays, during  
606 1300–1400 LT (1500–1600 LT for Zvenigorod), with those from OMI satellite observations  
607 (using the NASA algorithm). The reduction ratios for Yokosuka, Gwangju, and Zvenigorod  
608 for Sundays were 0.57, 0.89, and 0.71 for OMI, similar to 0.59, 0.76, and 0.85 for  
609 MAX-DOAS. On Saturdays, the reduction ratios were commonly larger, and were almost  
610 unity at Zvenigorod. The ratios for MAX-DOAS at Hefei were somewhat larger, but this  
611 could be a result of the small number of data available for this specific hour.

612

### 613 **3.3 Comparison with model simulations**

614 The climatology based on the TropoNO<sub>2</sub>VCD values observed with MAX-DOAS at Cape  
615 Hedo and Fukue, relatively remote locations, was compared with the simulation results  
616 derived from a global chemical transport model, MIROC-ESM-CHEM (Watanabe et al.,  
617 2012), based on CHASER (Sudo et al., 2002), to evaluate the model simulations. The model  
618 included stratospheric/tropospheric chemistry and aerosol schemes, and had a spatial  
619 resolution of 2.8° × 2.8° and 32 vertical layers. The wind field was assimilated using National  
620 Centers for Environmental Prediction data. HadISST/ICE  
621 ([http://badc.nerc.ac.uk/view/badc.nerc.ac.uk\\_\\_ATOM\\_\\_dataent\\_hadisst](http://badc.nerc.ac.uk/view/badc.nerc.ac.uk__ATOM__dataent_hadisst)) data were used for  
622 the sea surface temperature. The simulations were made for 6 years (2007–2012) and the  
623 average seasonal and diurnal variations were compared with the observations. The used  
624 emission inventory was derived from Cofala et al. (2007), but the baseline year was updated



625 to 2005. The  $\text{NO}_x$  emissions and concentrations in East Asia could therefore be  
626 underestimated for the study period, because the emission rates have increased since 2005.

627 In Fig. 17, seasonal variations in TropoNO<sub>2</sub>VCD at different sites during 1300–1400 LT are  
628 compared. For Cape Hedo, the concentrations in all seasons except winter were quite well  
629 reproduced by the model simulations. To our knowledge, this is the first use of the  
630 climatology of TropoNO<sub>2</sub>VCD values in such a low range, as observed at remote islands, to  
631 evaluate global chemical transport model simulations. The seasonal variations, with  
632 summertime minima and wintertime maxima, were also well reproduced, although the model  
633 tended to underestimate wintertime values. Similar features were observed in the comparison  
634 with Fukue Island (Fig. 17b), where the wintertime underestimation was more significant than  
635 that for Cape Hedo. Because Fukue Island is located nearer to  $\text{NO}_x$  source regions in the  
636 Asian continent (including the Korean Peninsula), possible underestimation of  $\text{NO}_x$  emissions  
637 on the continent could explain the differences during the winter, when air masses generally  
638 originate from the Asian continent. In contrast, during summer, clean air masses reached the  
639 two sites from the open Pacific Ocean. Our results therefore suggested that the model  
640 simulation is valid in summer under such conditions, where the TropoNO<sub>2</sub>VCD values were  
641 as low as  $0.6\text{--}1.5 \times 10^{15}$  molecules  $\text{cm}^{-2}$ .

642 Figure 18 compares the observed and modeled diurnal variations of TropoNO<sub>2</sub>VCD during  
643 four seasons. At Cape Hedo, the concentrations and detailed diurnal patterns, including  
644 daytime decreases and their rates in June–August (JJA) and September–November (SON),  
645 were almost perfectly reproduced by the model simulations. For Fukue, the rate of decrease at  
646 midday in JJA was also well captured by the model. This analysis again indicated that the  
647  $\text{NO}_2$  chemistry during the daytime was well simulated in the model, especially in summer.

648

### 649 **3.4 Data availability**

650 Numerical data files for the MADRAS network observations are available at

651 <http://eberpa.jamstec.go.jp/maxdoashp>. The files include TropoNO<sub>2</sub>VCD, AOD, vertical  
652 profiles of NO<sub>2</sub>, and extinction coefficients, with a 1-km resolution (up to 3 km) and a time  
653 resolution of 30 min. The color index information is also included (see the supplementary  
654 material for details).

655

#### 656 **4 Summary**

657 Long-term network observations of TropoNO<sub>2</sub>VCD were conducted at seven sites, in Japan,  
658 Korea, China, and Russia, covering remote to urban areas, from 2007, using standardized  
659 MAX-DOAS instruments. A single algorithm was applied to the raw spectra obtained at the  
660 sites to derive the  $\Delta$ SCDs of NO<sub>2</sub> and O<sub>4</sub>, and to estimate TropoNO<sub>2</sub>VCD optimally, using the  
661 aerosol information derived from the O<sub>4</sub> observations. A large number (>80,000) of the  
662 TropoNO<sub>2</sub>VCD values were used to test satellite observations of TropoNO<sub>2</sub>VCD from OMI  
663 and model simulations, and to investigate the climatology of NO<sub>2</sub>. The results were similar for  
664 two satellite data products with different retrieval algorithms (DOMINO ver. 2.0 and NASA  
665 ver. 2.1); the satellite observations had low biases, i.e., ~50%, whereas they were tightly  
666 correlated with the MAX-DOAS observations and showed closely matching seasonalities.  
667 Our analysis showed that the low biases could be attributed to the inhomogeneity of NO<sub>2</sub> on  
668 the spatial scale of the data products from OMI observations, and incomplete accounting for  
669 NO<sub>2</sub> present near the surface, possibly related to the shielding effect caused by the co-existing  
670 aerosols, for the satellite observations. Future satellite observations with smaller footprint  
671 sizes may help distinguishing the causes.

672 The average diurnal variations in TropoNO<sub>2</sub>VCD generally showed daytime decreases  
673 during the summer but increases during the winter at urban/suburban sites. Weekend  
674 reductions in NO<sub>2</sub> were clearly seen at Yokosuka and Gwangju, as a result of a reduction in  
675 the amount of traffic, but did not occur at Hefei, China, where the major emitting sector was  
676 probably different. The diurnal and weekly cyclic patterns at Yokosuka were in good

677 agreement with those derived from ground-based-monitoring data recorded near the site. A  
678 global chemical transport model, MIROC-ESM-CHEM, was validated for the first time with  
679 respect to background-level NO<sub>2</sub> column densities at Cape Hedo and Fukue during the  
680 summer, under the influence of marine air masses from the Pacific Ocean.

681

## 682 **Acknowledgments**

683 We thank Prede Co., Ltd. for technical assistance in developing instruments. Support from Y.  
684 Takeda and M. Kubo at the observatory is gratefully acknowledged. Drs. A. Takami and A.  
685 Shimizu (National Institute of Environmental Studies), T. Takamura (Chiba University), Y.  
686 Komazaki (Japan Agency for Marine and Earth Science and Technology) logistically  
687 supported our observations. We are grateful for free use of tropospheric NO<sub>2</sub> column data  
688 from the OMI sensor from [www.temis.nl](http://www.temis.nl) and from NASA. This work was supported by the  
689 Environmental Research and Technology Development Fund (S-7) of the Ministry of the  
690 Environment, Japan, by the Japan EOS Promotion Program (JEPP) and KAKENHI Grant  
691 numbers 25220101 and 26550022 of the Ministry of Education, Culture, Sports, Science, and  
692 Technology in Japan, by JSPS and RFBR (research project No. 12-05-92108\_Jap\_a and  
693 11-05-01175-a) under the Japan-Russia Research Cooperative Program, and by the GEMS  
694 program of the Ministry of Environment, Korea and the Eco Innovation Program of KEITI  
695 (2012000160004).

696

## 697 **References**

698 Beirle, S., Platt, U., Wenig, M., and Wagner, T.: Weekly cycle of NO<sub>2</sub> by GOME  
699 measurements: a signature of anthropogenic sources, *Atmos. Chem. Phys.*, 3, 2225-2232,  
700 2003.

701 Boersma, K. F., Eskes, H. J., Veefkind, J. P., Brinksma, E. J., van der A, R. J., Sneep, M., van  
702 den Oord, G. H. J., Levelt, P. F., Stammes, P., Gleason, J. F., and Bucsela, E. J.: Near-real  
703 time retrieval of tropospheric NO<sub>2</sub> from OMI, *Atmos. Chem. Phys.*, 7, 2103-2118,  
704 doi:10.5194/acp-7-2103-2007, 2007.

705 Boersma, K. F., Eskes, H. J., Dirksen, R. J., van der A, R. J., Veefkind, J. P., Stammes, P.,  
706 Huijnen, V., Kleipool, Q. L., Sneep, M., Claas, J., Leitão, J., Richter, A., Zhou, Y., and  
707 Brunner, D.: An improved tropospheric NO<sub>2</sub> column retrieval algorithm for the Ozone  
708 Monitoring Instrument, *Atmos. Meas. Tech.*, 4, 1905-1928, doi:10.5194/amt-4-1905-2011,  
709 2011.

710 Bogumil, K., Orphal, J., Homann, T., Voigt, S., Spietz, P., Fleischmann, O. C., Vogel, A.,  
711 Hartmann, M., Bovensmann, H., Frerik, J., and Burrows, J. P.: Measurements of molecular  
712 absorption spectra with the SCIAMACHY Pre-Flight Model: Instrument characterization  
713 and reference spectra for atmospheric remote sensing in the 230–2380 nm region, *J.*  
714 *Photochem. Photobiol. A.*, 157, 167–184, 2003.

715 Brinksma, E. J., Pinardi, G., Volten, H., Braak, R., Richter, A., Schönhardt, A., van  
716 Roozendaal, M., Fayt, C., Hermans, C., Dirksen, R. J., Vlemmix, T., Berkhout, A. J. C.,  
717 Swart, D. P. J., Oetjen, H., Wittrock, F., Wagner, T., Ibrahim, O. W., de Leeuw, G.,  
718 Moerman, M., Curier, R. L., Celarier, E. A., Cede, A., Knap, W. H., Veefkind, J. P., Eskes,  
719 H. J., Allaart, M., Rothe, R., PETERS, A. J. M., and Levelt, P. F.: The 2005 and 2006  
720 DANDELIONS NO<sub>2</sub> and aerosol intercomparison campaigns, *J. Geophys. Res.*, 113,  
721 D16S46, doi:10.1029/2007JD008808, 2008.

722 Bucsela, E. J., Perring, A. E., Cohen, R. C., Boersma, K. F., Celarier, E. A., Gleason, J. F.,  
723 Wenig, M. O., Bertram, T. J., Wookridge, P. J., Dirksen, R., and Veefkind, J. P.:  
724 Comparison of tropospheric NO<sub>2</sub> from in situ aircraft measurements with near-real-time  
725 and standard product data from OMI, *J. Geophys. Res.*, 113, D16S31,  
726 doi:10.1029/2007JD008838, 2008.

727 Bucsela, E. J., Krotkov, N. A., Celarier, E. A., Lamsal, L. N., Swartz, W. H., Bhartia, P. K.,  
728 Boersma, K. F., Veefkind, J. P., Gleason, J. F., and Pickering, K. E.: A new stratospheric  
729 and tropospheric NO<sub>2</sub> retrieval algorithm for nadir-viewing satellite instruments:  
730 applications to OMI, *Atmos. Meas. Tech.*, 6, 2607-2626, doi:10.5194/amt-6-2607-2013,  
731 2013.

732 Burrows, J. P., Weber, M., Buchwitz, M., Rozanov, V., Ladstätter-Weissenmayer, A., Richter,  
733 A., DeBeek, R., Hoogen, R., Bramstedt, K., Eichmann, K-U., Eisinger, M., and Perner, D.:  
734 Global ozone monitoring experiment (GOME): Mission concept and first scientific results,  
735 *J. Atmos. Sci.*, 56, 171-175, 1999.

736 Celarier, E. A., Brinksma, E. J., Gleason, J. F., Veefkind, J. P., Cede, A., Herman, J. R., Ionov,  
737 D., Goutail, F., Pommereau, J. -P., Lambert, J. -C., van Roozendaal, M., Pinardi, G.,  
738 Wittrock, F., Schönhardt, A., Richter, A., Ibrahim, O. W., Wagner, T., Bojkov, B., Mount, G.,  
739 Spinei, E., Chen, C. M., Pongetti, T. J., Sander, S. P., Bucsela, E. J., Wenig, M. O., Swart, D.  
740 P. J., Volten, H., Kroon, M., and Levelt, P. F.: Validation of Ozone Monitoring Instrument  
741 nitrogen dioxide columns, *J. Geophys. Res.*, 113, D15S15, doi:10.1029/2007JD008908,  
742 2008.

743 Chen, D., Zhou, B., Beirle, S., Chen, L. M., and Wagner, T.: Tropospheric NO<sub>2</sub> column

744 densities deduced from zenith-sky DOAS measurements in Shanghai, China, and their  
745 application to satellite validation, *Atmos. Chem. Phys.*, 9, 3641-3662,  
746 doi:10.5194/acp-9-3641-2009, 2009.

747 Clémer, K., Van Roozendael, M., Fayt, C., Hendrick, F., Hermans, C., Pinardi, G., Spurr, R.,  
748 Wang, P., and De Mazière, M.: Multiple wavelength retrieval of tropospheric aerosol  
749 optical properties from MAXDOAS measurements in Beijing, *Atmos. Meas. Tech.*, 3,  
750 863-878, 2010.

751 Cofala, J., Amann, M., Klimont, Z., Kupiainen, K., and Högund-Isaksson, L: Scenarios of  
752 global anthropogenic emissions of air pollutants and methane until 2030, *Atmos. Environ.*,  
753 41, 8486-8499, 2007.

754 Duce, R. A., LaRoche, J., Altieri, K., Arrigo, K. R., Baker, A. R., Capone, D. G., Cornell, S.,  
755 Dentener, F., Galloway, J., Ganeshram, R. S., Geider, R. J., Jickells, T., Kuypers, M. M.,  
756 Langlois, R., Liss, P. S., Liu, S. M., Middelburg, J. J., Moore, C. M., Nickovic, S., Oschlies,  
757 A., Pedersen, T., Prospero, J., Schlitzer, R., Seitzinger, S., Sorensen, L. L., Uematsu, M.,  
758 Ulloa, O., Voss, M., Ward, B., and Zamora, L.: Impacts of Atmospheric Anthropogenic  
759 Nitrogen on the Open Ocean, *Science*, 320(5878), 893–897, 2008.

760 Fayt, C. and Van Roozendael, M.: QDOAS Software User Manual Version 2.00,  
761 <http://uv-vis.aeronomie.be/software/QDOAS/> (last access April 2012), 2012.

762 Galle, B., Johansson, M., Rivera, C., Zhang, Y., Kihlman, M., Kern, C., Lehmann, T., Platt, U.,  
763 Arellano, S., and Hidalgo, S.: Network for Observation of Volcanic and Atmospheric  
764 Change (NOVAC)—A global network for volcanic gas monitoring: Network layout and  
765 instrument description, *J. Geophys. Res.*, 115, D05304, doi:10.1029/2009JD011823, 2010.

766 Hains, J. C., Boersma, K. F., Kroon, M., Dirksen, R. J., Cohen, R. C., Perring, A. E., Bucsele,  
767 E., Volten, H., Swart, D. P. J., Richter, A., Wittrock, F., Schoenhardt, A., Wagner, T.,  
768 Ibrahim, O. W., van Roozendael, M., Pinardi, G., Gleason, J. F., Veeffkind, J. P., and Levelt,  
769 P.: Testing and improving OMI DOMINO tropospheric NO<sub>2</sub> using observations from the  
770 DANDELIONS and INTEX-B validation campaigns, *J. Geophys. Res.*, 115, D05301,  
771 doi:10.1029/2009JD012399, 2010.

772 Hendrick, F., Müller, J.-F., Clémer, K., De Mazière, M., Fayt, C., Hermans, C., Stavrakou, T.,  
773 Vlemmix, T., Wang, P., and Van Roozendael, M.: Four years of ground-based MAX-DOAS  
774 observations of HONO and NO<sub>2</sub> in the Beijing area, *Atmos. Chem. Phys. Discuss.*, 13,  
775 10621-10660, doi:10.5194/acpd-13-10621-2013, 2013.

776 Heue, K.-P., Richter, A., Bruns, M., Burrows, J. P., v. Friedeburg, C., Platt, U., Pundt, I.,  
777 Wang, P., and Wagner, T.: Validation of SCIAMACHY tropospheric NO<sub>2</sub>-columns with  
778 AMAXDOAS measurements, *Atmos. Chem. Phys.*, 5, 1039-1051,  
779 doi:10.5194/acp-5-1039-2005, 2005.

780 Holben, B.N., Tanre, D., Smirnov, A., Eck, T. F., Slutsker, I., Abuhassan, N., Newcomb, W.W.,  
781 Schafer, J., Chatenet, B., Lavenue, F., Kaufman, Y. J., Vande Castle, J., Setzer, A.,  
782 Markham, B., Clark, D., Frouin, R., Halthore, R., Karnieli, A., O'Neill, N. T., Pietras, C.,

783 Pinker, R. T., Voss, K., and Zibordi, G.: An emerging ground-based aerosol climatology:  
784 Aerosol Optical Depth from AERONET, *J. Geophys. Res.*, 106, 12 067-12 097, 2001.

785 Hönninger, G., von Friedeburg, C., and Platt, U.: Multi axis differential optical absorption  
786 spectroscopy (MAX-DOAS), *Atmos. Chem. Phys.*, 4, 231-254,  
787 doi:10.5194/acp-4-231-2004, 2004.

788 Huijnen, V., Eskes, H. J., Poupkou, A., Elbern, H., Boersma, K. F., Foret, G., Sofiev, M.,  
789 Valdebenito, A., Flemming, J., Stein, O., Gross, A., Robertson, L., D'Isidoro, M.,  
790 Kioutsioukis, I., Friese, E., Amstrup, B., Bergstrom, R., Strunk, A., Vira, J., Zyryanov, D.,  
791 Maurizi, A., Melas, D., Peuch, V.-H., and Zerefos, C.: Comparison of OMI NO<sub>2</sub>  
792 tropospheric columns with an ensemble of global and European regional air quality models,  
793 *Atmos. Chem. Phys.*, 10, 3273–3296, doi:10.5194/acp-10-3273-2010, 2010.

794 Irie, H., Kanaya, Y., Akimoto, H., Tanimoto, H., Wang, Z., Gleason, J. F., and Bucsele, E. J.:  
795 Validation of OMI tropospheric NO<sub>2</sub> column data using MAX-DOAS measurements deep  
796 inside the North China Plain in June 2006, *Atmos. Chem. Phys.*, 8, 6577-6586, 2008a.

797 Irie, H., Kanaya, Y., Akimoto, H., Iwabuchi, H., Shimizu, A., and Aoki, K.: First retrieval of  
798 tropospheric aerosol profiles using MAX-DOAS and comparison with lidar and sky  
799 radiometer measurements, *Atmos. Chem. Phys.*, 8, 341-350, 2008b.

800 Irie, H., Kanaya, Y., Takashima, H., Gleason, J. F., and Wang, Z.: Characterization of OMI  
801 tropospheric NO<sub>2</sub> measurements in East Asia based on a robust validation comparison,  
802 *SOLA*, 5, 117-120, 2009a.

803 Irie, H., Kanaya, Y., Akimoto, H., Iwabuchi, H., Shimizu, A., and Aoki, K.: Dual-wavelength  
804 aerosol vertical profile measurements by MAX-DOAS at Tsukuba, Japan, *Atmos. Chem.*  
805 *Phys.*, 9, 2741-2749, 2009b.

806 Irie, H., Takashima, H., Kanaya, Y., Boersma, K. F., Gast, L., Wittrock, F., Brunner, D., Zhou,  
807 Y., and Van Roozendaal, M.: Eight-component retrievals from ground-based MAX-DOAS  
808 observations, *Atmos. Meas. Tech.*, 4, 1027-1044, doi:10.5194/amt-4-1027-2011, 2011.

809 Irie, H., Boersma, K. F., Kanaya, Y., Takashima, H., Pan, X., and Wang, Z. F.: Quantitative  
810 bias estimates for tropospheric NO<sub>2</sub> columns retrieved from SCIAMACHY, OMI, and  
811 GOME-2 using a common standard, *Atmos. Meas. Tech.*, 5, 2403-2411,  
812 doi:10.5194/amt-5-2403-2012, 2012.

813 Iwabuchi, H.: Efficient Monte Carlo methods for radiative transfer modeling, *J. Atmos. Sci.*,  
814 63, 9, 2324–2339, 2006.

815 Kanaya, Y., Sadanaga, Y., Nakamura, K., and Akimoto, H.: Behavior of OH and HO<sub>2</sub> radicals  
816 during the Observations at a Remote Island of Okinawa (ORION99) field campaign: 1.  
817 Observation using a laser-induced fluorescence instrument, *J. Geophys. Res.*, 106(D20),  
818 24197–24208, doi:10.1029/2000JD000178, 2001.

819 Kannari, A., Tonooka, Y., Baba, T., Murano, K.: Development of multiple-species 1 km × 1 km  
820 m resolution hourly basis emissions inventory for Japan, *Atmos. Environ.*, 41, 3428-3439,  
821 2007.

822 Kondo, Y., Morino, Y., Fukuda, M., Kanaya, Y., Miyazaki, Y., Takegawa, N., Tanimoto, H.,  
823 McKenzie, R., Johnston, P., Blake, D. R., Murayama, T., and Koike, M.: Formation and  
824 transport of oxidized reactive nitrogen, ozone, and secondary organic aerosol in Tokyo, *J.*  
825 *Geophys. Res.*, 113, D21310, doi:10.1029/2008JD010134, 2008.

826 Lamsal, L. N., Martin, R. V., van Donkelaar, A., Celarier, E. A., Bucsela, E. J., Boersma, K.  
827 F., Dirksen, R., Luo, C., and Wang, Y.: Indirect validation of tropospheric nitrogen dioxide  
828 retrieved from the OMI satellite instrument: Insight into the seasonal variation of nitrogen  
829 oxides at northern midlatitudes, *J. Geophys. Res.*, 115, D05302,  
830 doi:10.1029/2009JD013351, 2010.

831 Leitão, J., Richter, A., Vrekoussis, M., Kokhanovsky, A., Zhang, Q. J., Beekmann, M., and  
832 Burrows, J. P.: On the improvement of NO<sub>2</sub> satellite retrievals – aerosol impact on the  
833 air mass factors, *Atmos. Meas. Tech.*, 3, 475-493, doi:10.5194/amt-3-475-2010, 2010.

834 Lin, J.-T., Martin, R. V., Boersma, K. F., Sneep, M., Stammes, P., Spurr, R., Wang, P., Van  
835 Roozendael, M., Clémer, K., and Irie, H.: Retrieving tropospheric nitrogen dioxide over  
836 China from the Ozone Monitoring Instrument: Effects of aerosols, surface reflectance  
837 anisotropy and vertical profile of nitrogen dioxide, *Atmos. Chem. Phys. Discuss.*,  
838 21203-21257, 2013.

839 Ma, J. Z., Beirle, S., Jin, J. L., Shaiganfar, R., Yan, P., and Wagner, T.: Tropospheric NO<sub>2</sub>  
840 vertical column densities over Beijing: results of the first three years of ground-based  
841 MAX-DOAS measurements (2008–2011) and satellite validation, *Atmos. Chem. Phys.*, 13,  
842 1547-1567, doi:10.5194/acp-13-1547-2013, 2013.

843 Martin, R. V., Sioris, C. E., Chance, K., Ryerson, T. B., Bertram, T. H., Wooldridge, P. J.,  
844 Cohen, R. C., Neuman, J. A., Swanson, A., and Flocke, F. M.: Evaluation of space-based  
845 constraints on global nitrogen oxide emissions with regional aircraft measurements over  
846 and downwind of eastern North America, *J. Geophys. Res.*, 111, D15308,  
847 doi:10.1029/2005JD006680, 2006.

848 Peters, E., Wittrock, F., Großmann, K., Frieß, U., Richter, A., and Burrows, J. P.:  
849 Formaldehyde and nitrogen dioxide over the remote western Pacific Ocean: SCIAMACHY  
850 and GOME-2 validation using ship-based MAX-DOAS observations, *Atmos. Chem. Phys.*,  
851 12, 11179-11197, doi:10.5194/acp-12-11179-2012, 2012.

852 Piters, A. J. M., Boersma, K. F., Kroon, M., Hains, J.C., Van Roozendael, M., Wittrock, F.,  
853 Abuhassan, N., Adams, C., Akrami, M., Allaart, M. A. F., Apituley, A., Beirle, S., Bergwerff,  
854 J. B., Berkhout, A. J. C., Brunner, D., Cede, A., Chong, J., Clémer, K., Fayt, C., Frieß, U.,  
855 Gast, L. F. L., Gil-Ojeda, M., Goutail, F., Graves, R., Griesfeller, A., Großmann, K.,  
856 Hemerijckx, G., Hendrick, F., Henzing, B., Herman, J., Hermans, C., Hoexum, M., van der  
857 Hoff, G. R., Irie, H., Johnston, P. V., Kanaya, Y., Kim, Y. J., Klein Baltink, H., Kreher, K.,  
858 de Leeuw, G., Leigh, R., Merlaud, A., Moerman, M. M., Monks, P. S., Mount, G. H.,  
859 Navarro-Comas, M., Oetjen, H., Pazmino, A., Perez-Camacho, M., Peters, E., du Piesanie,  
860 A., Pinardi, G., Puentedura, O., Richter, A., Roscoe, H. K., Schönhardt, A., Schwarzenbach,

861 B., Shaiganfar, R., Sluis, W., Spinei, E., Stolk, A. P., Strong, K., Swart, D. P. J., Takashima,  
862 H., Vlemmix, T., Vrekoussis, M., Wagner, T., Whyte, C., Wilson, K. M., Yela, M., Yilmaz,  
863 S., Zieger, P., and Zhou, Y.: The Cabauw Intercomparison campaign for Nitrogen Dioxide  
864 measuring Instruments (CINDI): design, execution, and early results, *Atmos. Meas. Tech.*,  
865 5, 457-485, doi:10.5194/amt-5-457-2012, 2012.

866 Platt, U., Differential optical absorption spectroscopy (DOAS), *Chem. Anal. Series*, 127, 27-  
867 83, 1994.

868 Richter, A., Burrows, J. P., Nuss, H., Granier, C., and Niemeier, U.: Increase in tropospheric  
869 nitrogen dioxide over China observed from space, *Nature*, 437, 129–132, 2005.

870 Rodgers, C. D.: Inverse methods for atmospheric sounding: Theory and practice, *Ser. Atmos.*  
871 *Oceanic Planet. Phys.*, 2, edited by F. W. Taylor, World Sci., Hackensack, N. J., 2000.

872 Roscoe, H. K., Van Roozendaal, M., Fayt, C., du Piesanie, A., Abuhassan, N., Adams, C.,  
873 Akrami, M., Cede, A., Chong, J., Clémer, K., Friess, U., Gil Ojeda, M., Goutail, F., Graves,  
874 R., Griesfeller, A., Grossmann, K., Hemerijckx, G., Hendrick, F., Herman, J., Hermans, C.,  
875 Irie, H., Johnston, P. V., Kanaya, Y., Kreher, K., Leigh, R., Merlaud, A., Mount, G. H.,  
876 Navarro, M., Oetjen, H., Pazmino, A., Perez-Camacho, M., Peters, E., Pinardi, G.,  
877 Puentedura, O., Richter, A., Schönhardt, A., Shaiganfar, R., Spinei, E., Strong, K.,  
878 Takashima, H., Vlemmix, T., Vrekoussis, M., Wagner, T., Wittrock, F., Yela, M., Yilmaz, S.,  
879 Boersma, F., Hains, J., Kroon, M., Piters, A., and Kim, Y. J.: Intercomparison of slant  
880 column measurements of NO<sub>2</sub> and O<sub>4</sub> by MAX-DOAS and zenith-sky UV and visible  
881 spectrometers, *Atmos. Meas. Tech.*, 3, 1629-1646, doi:10.5194/amt-3-1629-2010, 2010.

882 Rothman, L. S., Barbe, A., Chris Benner, D., and Hitran-Team.: The HITRAN Molecular  
883 Spectroscopic Database: Edition of 2000 including updates through 2001, *J. Quant.*  
884 *Spectrosc. Radiat. Transfer*, 82, 5–44, 2003.

885 Shaiganfar, R., Beirle, S., Sharma, M., Chauhan, A., Singh, R. P., and Wagner, T.: Estimation  
886 of NO<sub>x</sub> emissions from Delhi using Car MAX-DOAS observations and comparison with  
887 OMI satellite data, *Atmos. Chem. Phys.*, 11, 10871-10887, doi:10.5194/acp-11-10871-2011,  
888 2011.

889 Sinreich, R., Frieß, U., Wagner, T., and Platt, U.: Multi axis differential optical absorption  
890 spectroscopy (MAX-DOAS) of gas and aerosol distributions, *Faraday Discussions*, 130,  
891 153-164, doi: 10.1039/b419274p, 2005.

892 Sudo, K., Takahashi, M., Kurokawa, J., and Akimoto, H.: CHASER: A global chemical  
893 model of the troposphere 1. Model description, *J. Geophys. Res.*, 107 (D17), 4339,  
894 doi:10.1029/2001JD001113, 2002.

895 Takami, A., Miyoshi, T., Shimono, A., Kaneyasu, N., Kato, S., Kajii, Y., and Hatakeyama, S.:  
896 Transport of anthropogenic aerosols from Asia and subsequent chemical transformation, *J.*  
897 *Geophys. Res.*, 112, D22S31, doi:10.1029/2006JD008120, 2007.

898 Takashima, H., Irie, H., Kanaya, Y., Shimizu, A., Aoki, K., and Akimoto, H.: Atmospheric  
899 aerosol variations at Okinawa Island in Japan observed by MAX-DOAS using a new



900 cloud-screening method, *J. Geophys. Res.*, 114, D18213, doi:10.1029/2009JD011939,  
901 2009.

902 Takashima, H., Irie, H., Kanaya, Y., and Akimoto, H.: Enhanced NO<sub>2</sub> at Okinawa Island,  
903 Japan caused by rapid air mass transport from China as observed by MAX-DOAS, *Atmos.*  
904 *Environ.*, 45(15), 2593-2597, 2011.

905 Takashima, H., Irie, H., Kanaya, Y., and Syamsudin, F.: NO<sub>2</sub> observations over the western  
906 Pacific and Indian Ocean by MAX-DOAS on Kaiyo, a Japanese research vessel, *Atmos.*  
907 *Meas. Tech.* 5, 2351-2360, doi: 10.5194/amt-5-2351-2012, 2012.

908 Theys, N., Van Roozendael, M., Hendrick, F., Fayt, C., Hermans, C., Baray, J.-L., Goutail, F.,  
909 Pommereau, J.-P., and e Mazière, M. D: Retrieval of stratospheric and tropospheric BrO  
910 columns from Multi-Axis DOAS measurements at Reunion Island (21°S, 56°E), *Atmos.*  
911 *Chem. Phys.*, 7, 4733-4749, 2007.

912 Valks, P., Pinardi, G., Richter, A., Lambert, J.-C., Hao, N., Loyola, D., Van Roozendael, M.,  
913 and Emmadi, S.: Operational total and tropospheric NO<sub>2</sub> column retrieval for GOME-2,  
914 *Atmos. Meas. Tech.*, 4, 1491-1514, doi:10.5194/amt-4-1491-2011, 2011.

915 Vandaele, A. C., Hermans, C., Simon, P. C., Van Roozendael, M., Guilmot, J. M., Carleer, M.,  
916 and Colin, R.: Fourier transform measurement of NO<sub>2</sub> absorption cross-section in the  
917 visible range at room temperature, *J. Atmos. Chem.*, 25, 289–305, 1996.

918 van der A, R. J., Eskes, H. J., Boersma, K. F., van Noije, T. P. C., Van Roozendael, M., De  
919 Smedt, I., Peters, D. H. M. U., and Meijer, E. W.: Trends, seasonal variability and  
920 dominant NO<sub>x</sub> source derived from a ten year record of NO<sub>2</sub> measured from space, *J.*  
921 *Geophys. Res.*, 113, D04302, doi:10.1029/2007JD009021, 2008.

922 Wagner, T., Burrows, J. P., Deutschmann, T., Dix, B., von Friedeburg, C., Frieß, U.,  
923 Hendrick, F., Heue, K.-P., Irie, H., Iwabuchi, H., Kanaya, Y., Keller, J., McLinden, C. A.,  
924 Oetjen, H., Palazzi, E., Petritoli, A., Platt, U., Postlyakov, O., Pukite, J., Richter, A., van  
925 Roozendael, M., Rozanov, A., Rozanov, V., Sinreich, R., Sanghavi, S., and Wittrock, F.:  
926 Comparison of box-air-mass-factors and radiances for Multiple-Axis Differential Optical  
927 Absorption Spectroscopy (MAX-DOAS) geometries calculated from different UV/visible  
928 radiative transfer models, *Atmos. Chem. Phys.*, 7, 1809-1833,  
929 doi:10.5194/acp-7-1809-2007, 2007.

930 Watanabe, S., Takemura, T., Sudo, K., Yokohata, T., and Kawase, H.: Anthropogenic  
931 changes in the surface all-sky UV-B radiation through 1850–2005 simulated by an Earth  
932 system model, *Atmos. Chem. Phys.*, 12, 5249-5257, doi:10.5194/acp-12-5249-2012, 2012.

933 Wenig, M. O., Cede, A. M., Bucsela, E. J., Celarier, E. A., Boersma, K. F., Veefkind, J. P.,  
934 Brinksma, E. J., Gleason, J. F., and Herman, J. R.: Validation of OMI tropospheric NO<sub>2</sub>  
935 column densities using direct-Sun mode Brewer measurements at NASA Goddard Space  
936 Flight Center, *J. Geophys. Res.*, 113, D16S45, doi:10.1029/2007JD008988, 2008.

937 Wittrock, F., Oetjen, H., Richter, A., Fietkau, S., Medeke, T., Rozanov, A., and Burrows, J. P.:  
938 MAX-DOAS measurements of atmospheric trace gases in Ny-Ålesund - Radiative transfer

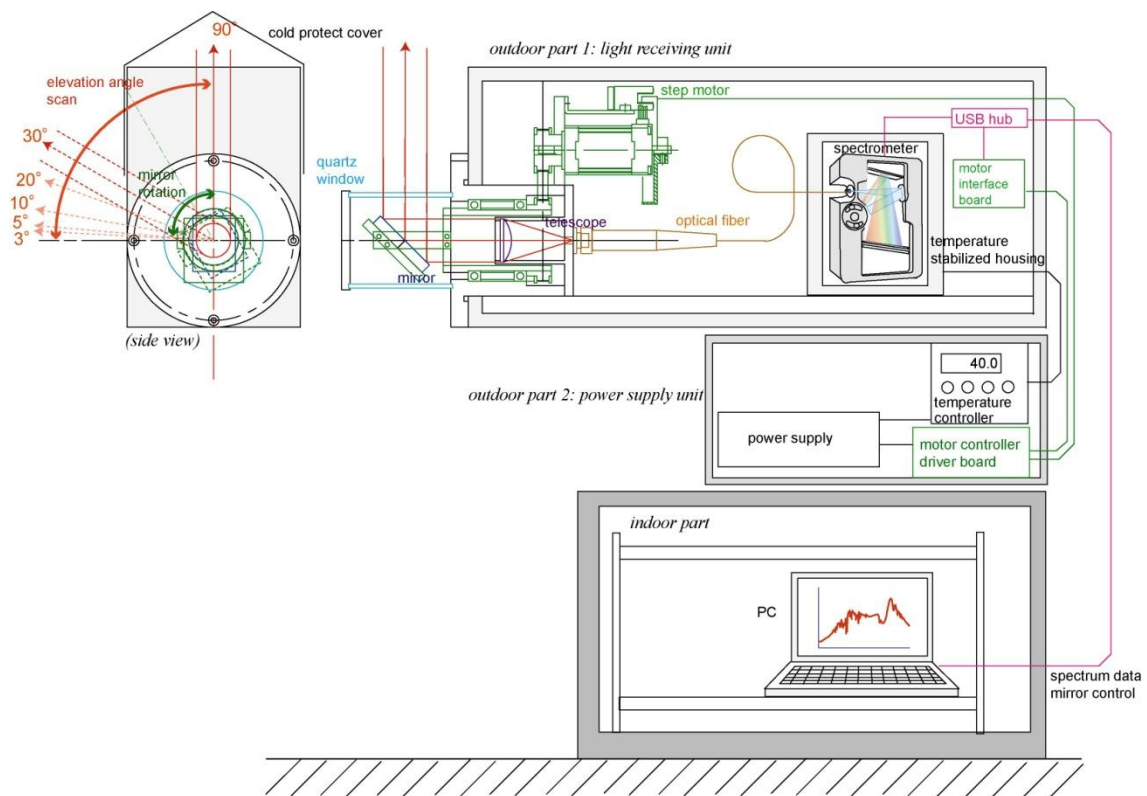
939 studies and their application, *Atmos. Chem. Phys.*, 4, 955-966, 2004  
940 Yurganov, L., McMillan, W., Grechko, E., and Dzhola, A., Analysis of global and regional CO  
941 burdens measured from space between 2000 and 2009 and validated by ground-based solar  
942 tracking spectrometers, *Atmos. Chem. Phys.*, 10, 3479–3494, 2010.  
943 Zhang, Q., Streets, D. G., Carmichael, G. R., He, K. B., Huo, H., Kannari, A., Klimont, Z.,  
944 Park, I. S., Reddy, S., Fu, J. S., Chen, D., Duan, L., Lei, Y., Wang, L. T., and Yao, Z. L.:  
945 Asian emissions in 2006 for the NASA INTEX-B mission, *Atmos. Chem. Phys.*, 9,  
946 5131-5153, doi:10.5194/acp-9-5131-2009, 2009.  
947 Zhou, Y., Brunner, D., Boersma, K. F., Dirksen, R., and Wang, P.: An improved tropospheric  
948 NO<sub>2</sub> retrieval for OMI observations in the vicinity of mountainous terrain, *Atmos. Meas.*  
949 *Tech.*, 2, 401–416, doi:10.5194/amt-2-401-2009, 2009.

950

951

**Table 1.** List of locations for MAX-DOAS observations.

952	Location	Type	Latitude (°N)	Longitude (°E)	Surface Elevation (m)	Instrument Elevation (m)	Azimuth angle (°, from North, clockwise)	N (NO <sub>2</sub> retrievals)	Instruments and used periods
953	Yokosuka	Urban	35.32	139.65	0	10	+37	26,554	#1 (Type A), Apr 2007–Dec 2012
	Cape Hedø	Remote	26.87	128.25	0	68	−14	18,367	#1 (Type A), Mar 2007–Dec 2012
954	Gwangju	Suburban	35.23	126.84	30	43	+44	11,349	#1 (Type C), Feb 2008–Jun 2009 #2 (Type C), Nov 2009–Aug 2010 #3 (Type B), May 2011–Dec 2012
955	Hefei	Suburban	31.91	117.16	30	51	+22	5,324	#1 (Type C), Mar 2008–Oct 2009 #2 (Type C), Nov 2009–Dec 2012
956	Zvenigorod	Rural	55.70	36.78	186	208	−32	8,948	#1 (Type C), Oct 2008–Dec 2012
	Tomsk	Suburban	56.48	85.05	160	188	0	-	#1 (Type C), Jan 2009–Dec 2012
957	Fukue	Remote	32.75	128.68	80	83	+30	10,385	#1 (Type B), Mar 2009–Apr 2009 #2 (Type C), Apr 2009–Mar 2012 #3 (Type B), Mar 2012–Dec 2012
	<b>TOTAL</b>							<b>80,927</b>	



958

959 **Fig. 1.** Schematic diagram of MAX-DOAS instrument used at Zvenigorod.

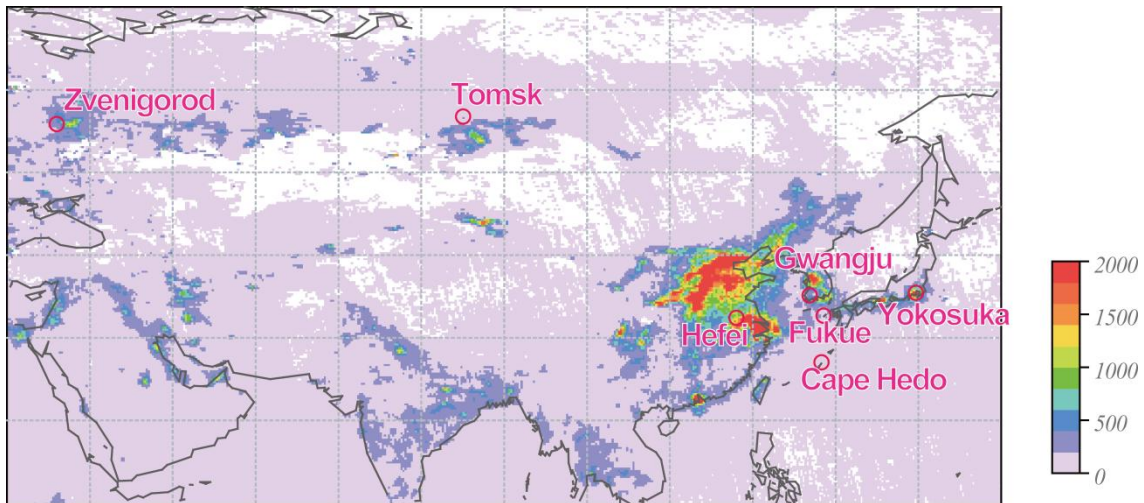


960

961

962 **Fig. 2.** Two horizontal levels embedded in the base plate (upper arrow) and in a plate holding  
963 the reflecting mirror (lower arrow) were used to adjust the zero angle of the reflecting mirror.

964



965

966 **Fig. 3.** Locations of our MAX-DOAS observations. The background contour is based on the

967 TropoNO<sub>2</sub>VCD (10<sup>13</sup> molecules cm<sup>-2</sup>) observed by OMI (DOMINO ver. 2.0).

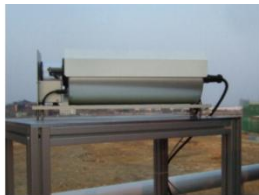
968



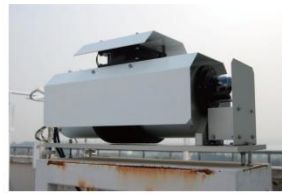
Yokosuka



Cape Hedo



Gwangju



Hefei



Fukue



Tomsk

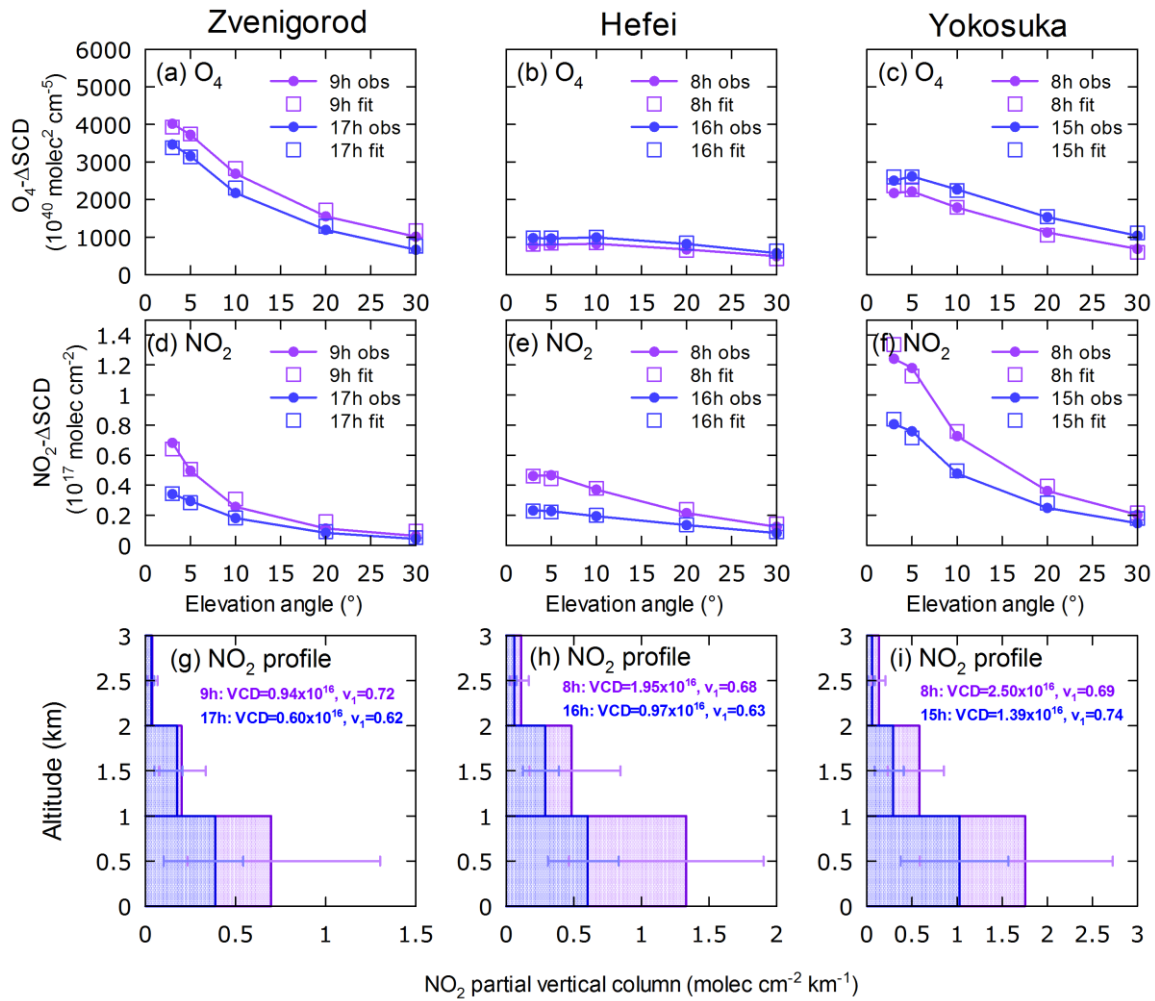


Zvenigorod

969

970 **Fig. 4.** Light-receiving parts of MAX-DOAS instruments located at the seven sites.

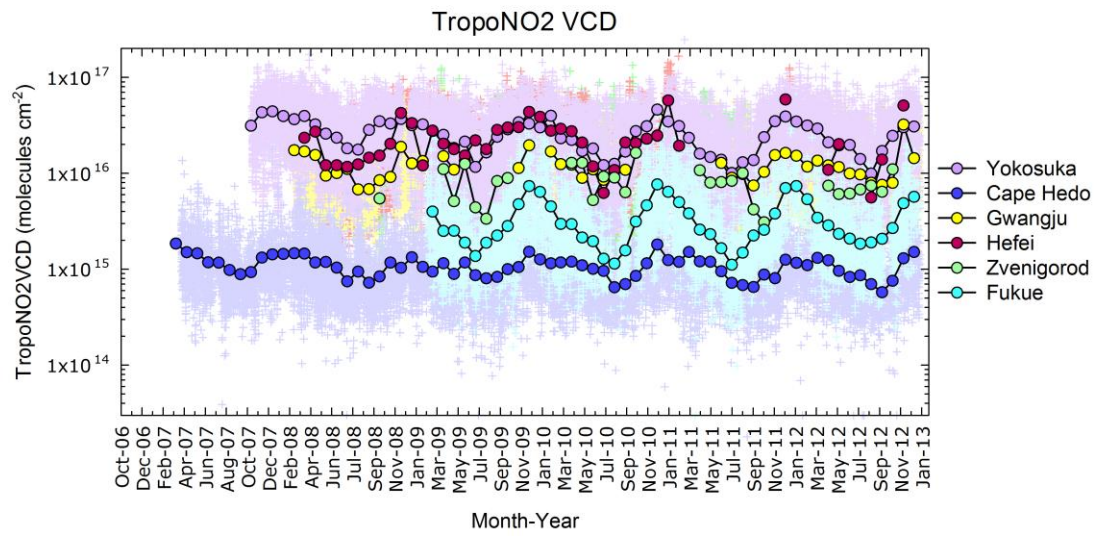
971



972

973 **Fig. 5.** (a)–(f) Observed and fitted O<sub>4</sub> ΔSCDs and NO<sub>2</sub> ΔSCDs, and (g)–(i) optimally  
 974 estimated NO<sub>2</sub> vertical profiles averaged over each 1-h period in the morning and afternoon  
 975 at Zvenigorod, Hefei, and Yokosuka sites, respectively. For (g)–(i), error bars represent 1σ  
 976 range of individual profiles included in the hours.



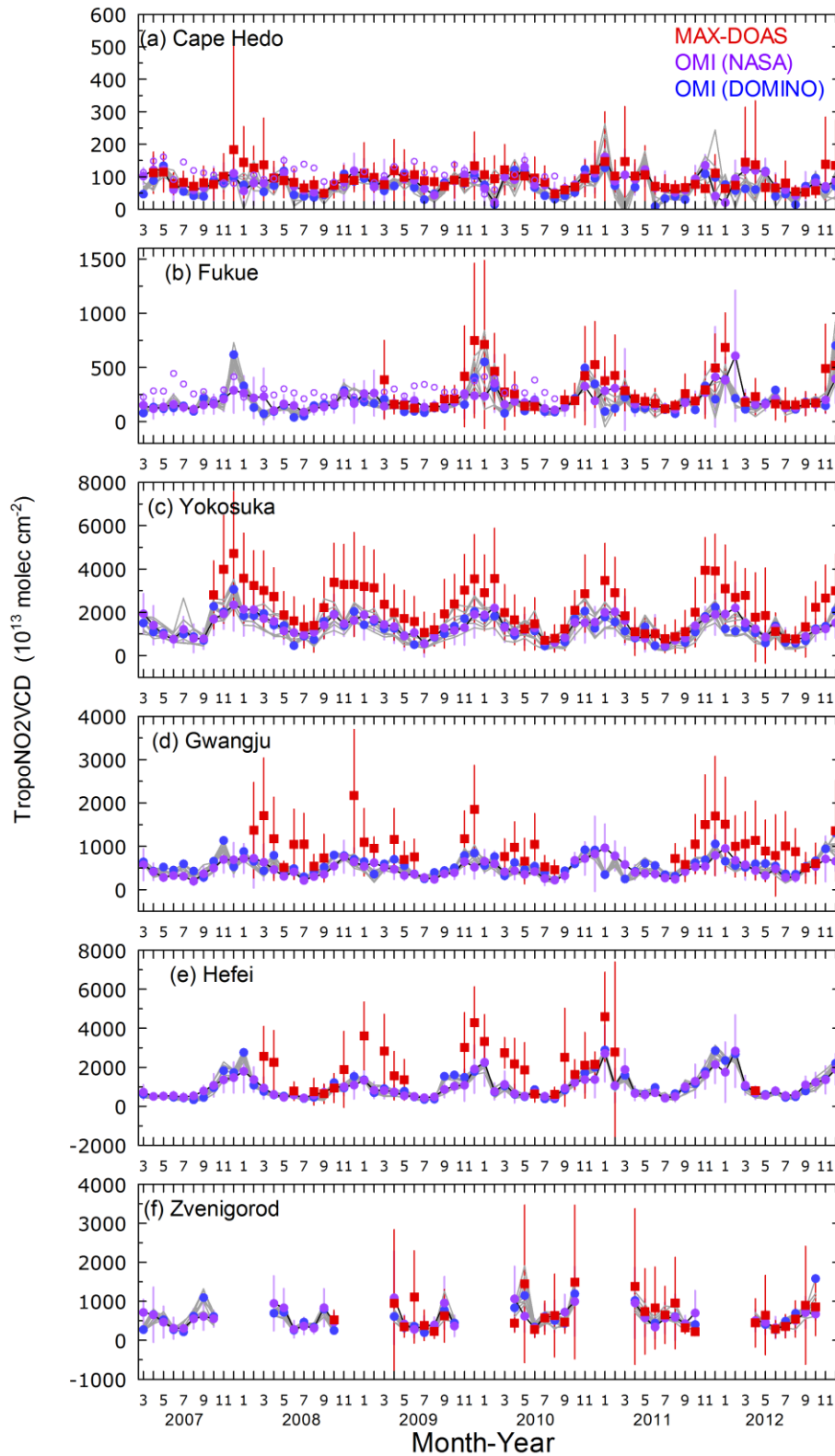


977

978

979 **Fig. 6.** Time series of all individual observations of TropoNO<sub>2</sub>VCD (plus signs, 30-min time  
 980 resolution) and their monthly averages (circles).

981



982

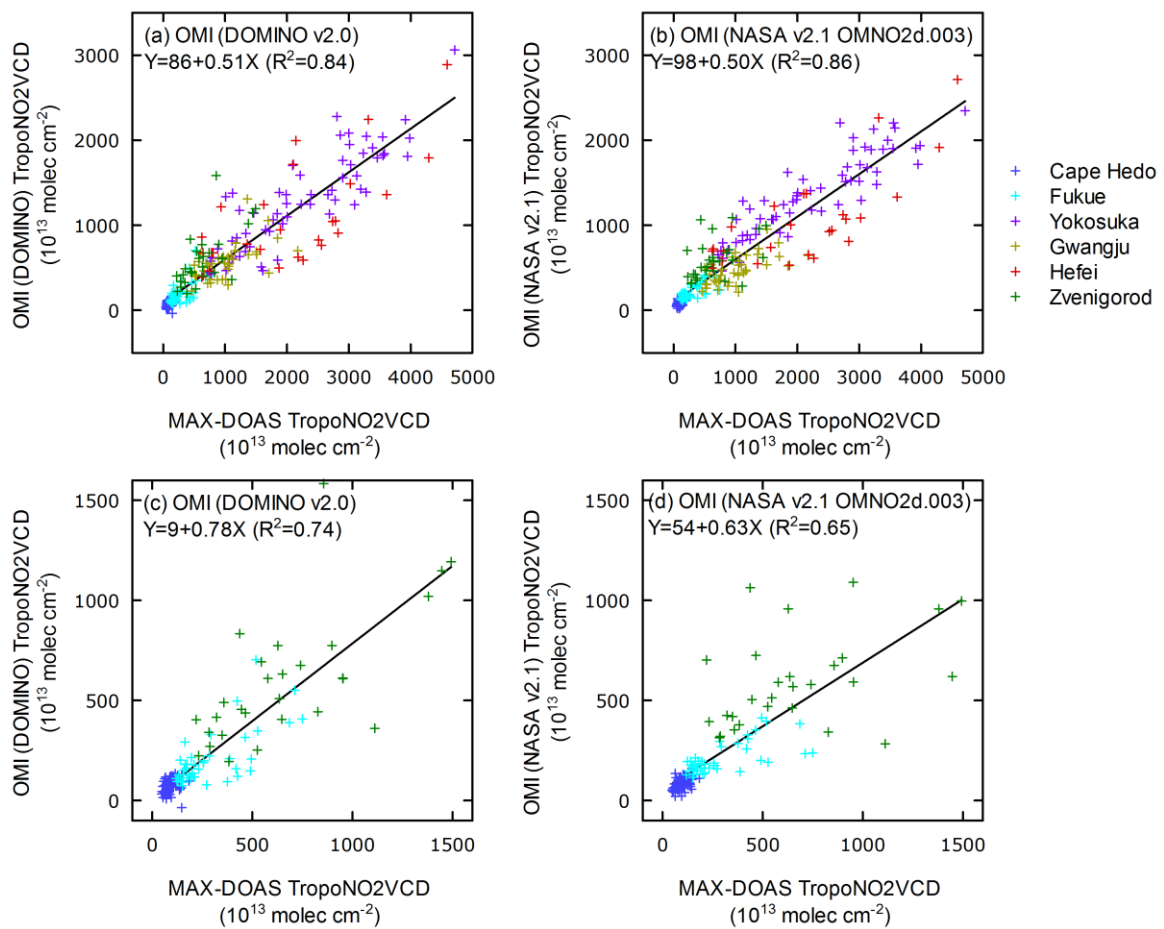
983 **Fig. 7.** Time series of monthly averages of MAX-DOAS (red) and satellite observations of

984 TropoNO<sub>2</sub>VCD. The satellite observations are derived using NASA (ver. 2.1, purple) and

985 DOMINO (ver. 2.0, blue) algorithms. Open purple circles in (a) and (b) represent data from

986 older products (NASA ver. 1). Error bars of MAX-DOAS represent  $1\sigma$  ranges of included  
987 data. Error bars of OMI with NASA ver. 2.1 algorithm were calculated from  $1\sigma$  ranges of  
988 daily data included in the month. Gray lines represent OMI data using DOMINO ver. 2.0  
989 algorithm at the eight grids ( $0.125^\circ \times 0.125^\circ$ ) adjacent to the grid nearest the site (blue  
990 circles).

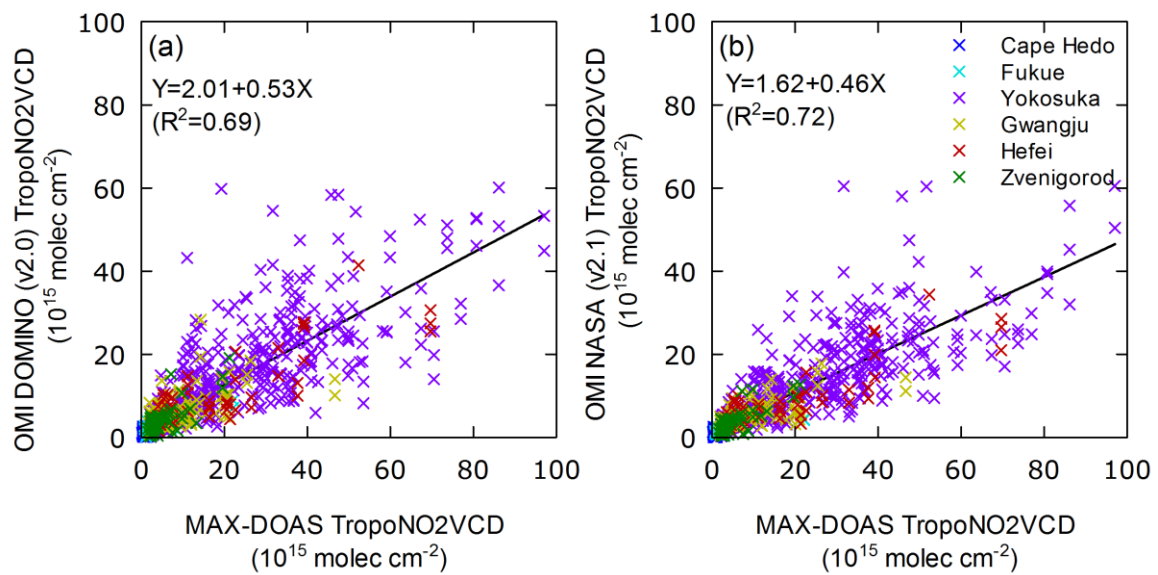
991



992

993 **Fig. 8.** Scatterplots between monthly averages of TropoNO<sub>2</sub>VCD derived from OMI and  
 994 MAX-DOAS for (a) and (b) all sites, and for (c) and (d) three rural/remote sites, using  
 995 DOMINO ver. 2.0 for (a) and (c), and NASA ver. 2.1 for (b) and (d).

996



997

998 **Fig. 9.** Similar to Fig. 8 but for pixel-based comparisons with strict coincidence criteria

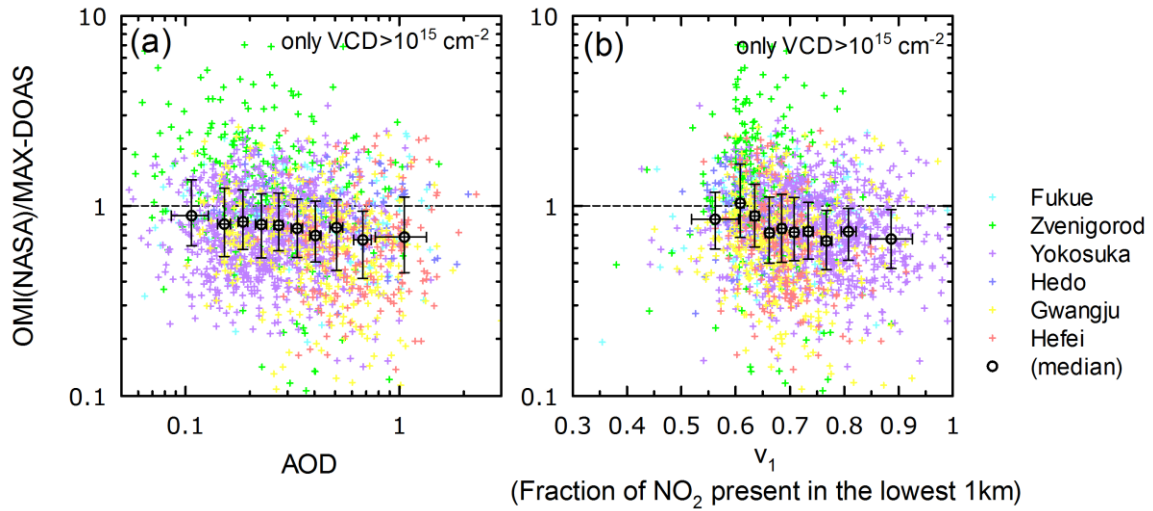
999 (horizontal displacement  $<0.15^\circ$ , time difference  $<15$  min), and cloud screening (cloud

1000 fraction  $<10\%$ ); DOMINO (ver. 2.0) and NASA (ver. 2.1) were used for (a) and (b),

1001 respectively.

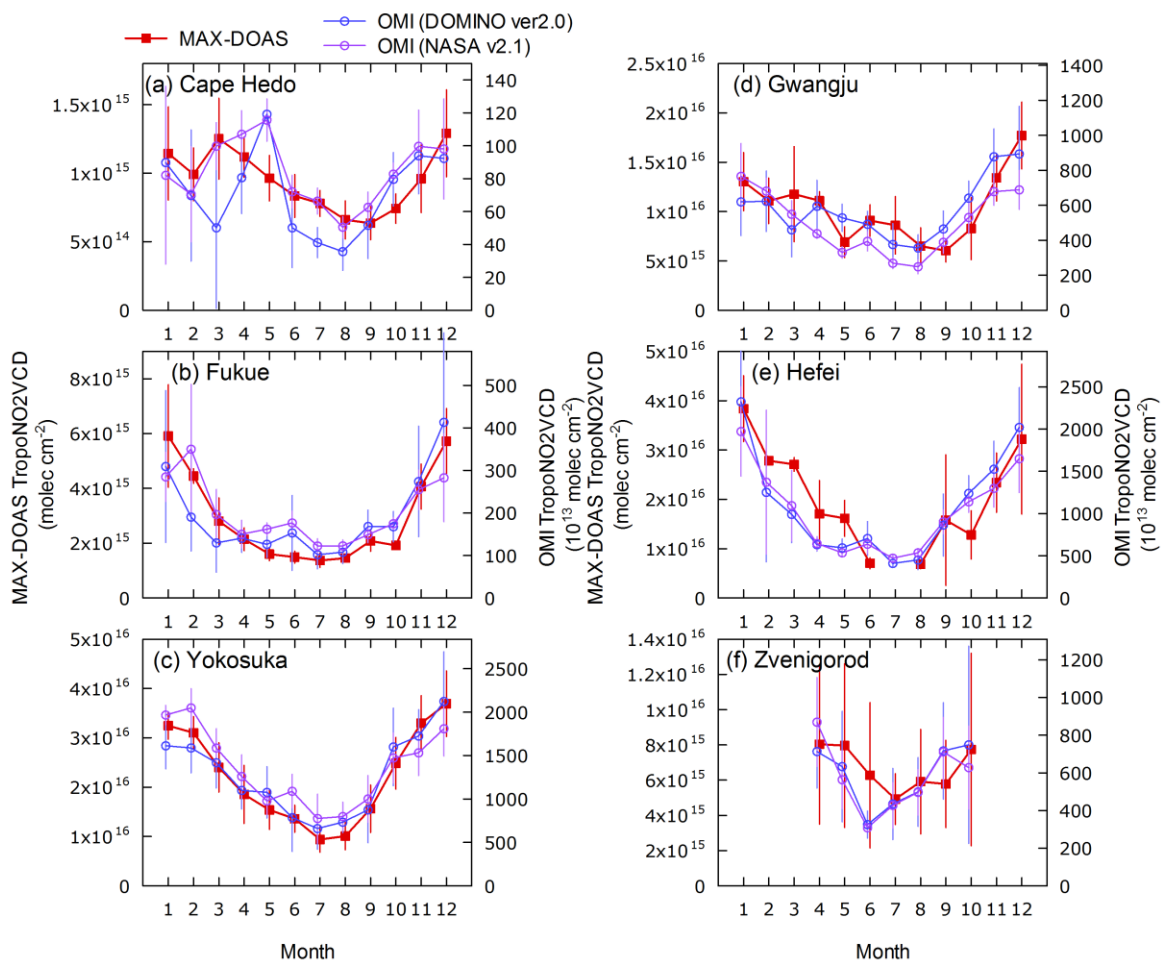
1002

1003



1004

1005 **Fig. 10.** OMI(NASA)/MAX-DOAS ratios for TropoNO<sub>2</sub>VCD were plotted against (a) AOD  
 1006 at 476 nm, observed with MAX-DOAS and (b)  $v_1$ , a retrieved parameter defining the fraction  
 1007 of NO<sub>2</sub> present in the lowest 1 km. Black circles and error bars represent the median ratios  
 1008 and  $1\sigma$  ranges for the 10 bins sorted by AOD and  $v_1$ , respectively.



1009

1010

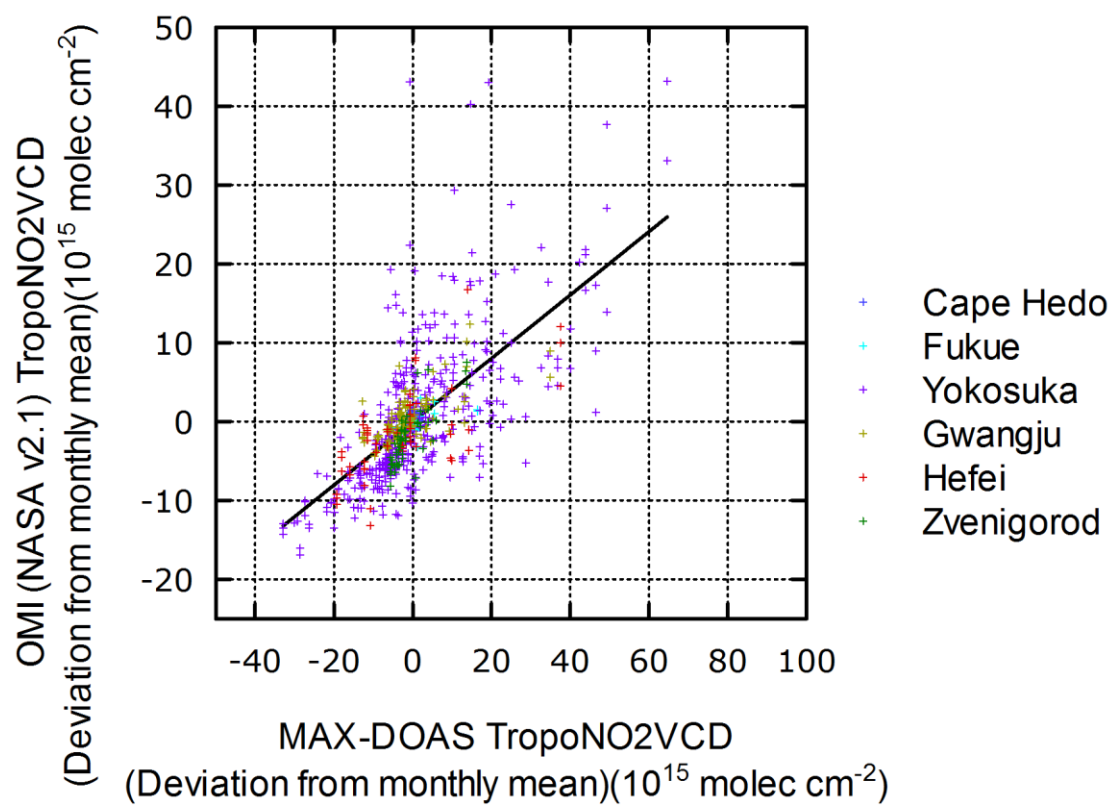
1011 **Fig. 11.** Seasonality comparisons for TropoNO<sub>2</sub>VCD values derived from MAX-DOAS and

1012 satellite observations. MAX-DOAS data from the hours of satellite observations were used.

1013 The error bars represent variability in the monthly average TropoNO<sub>2</sub>VCD values over the

1014 studied years.

1015

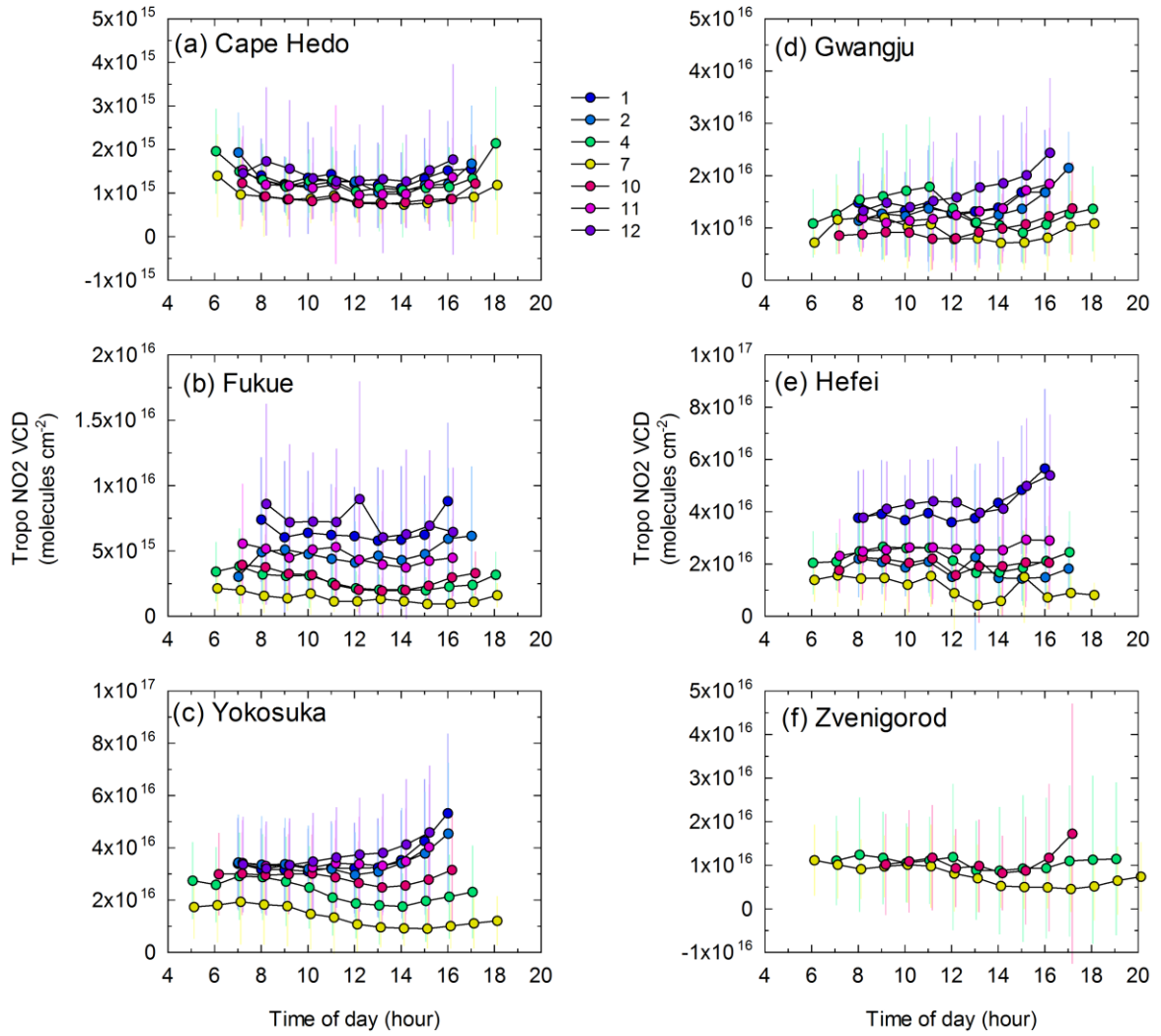


1016

1017 **Fig. 12.** Same as Fig. 9b but deviations from monthly mean values were plotted.

1018





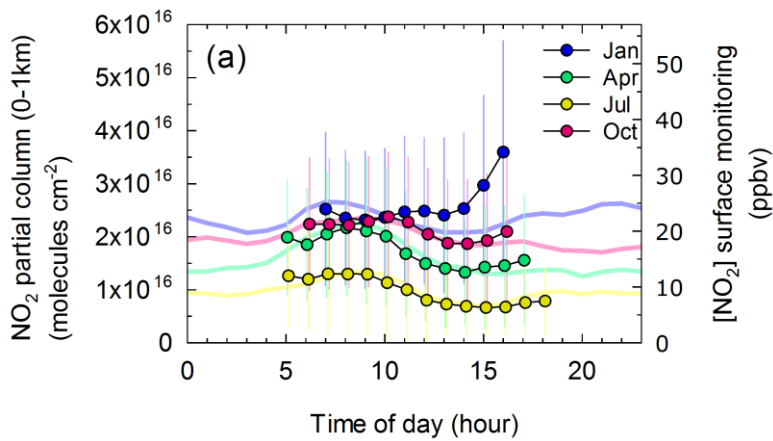
1019

1020 **Fig. 13.** Average diurnal variations in TropoNO<sub>2</sub>VCD for selected months (differently

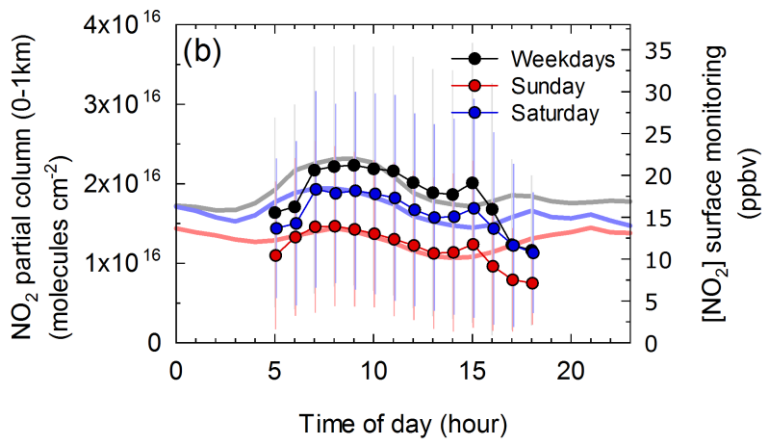
1021 colored). Error bars represent the 1σ range of the included data.

1022

1023



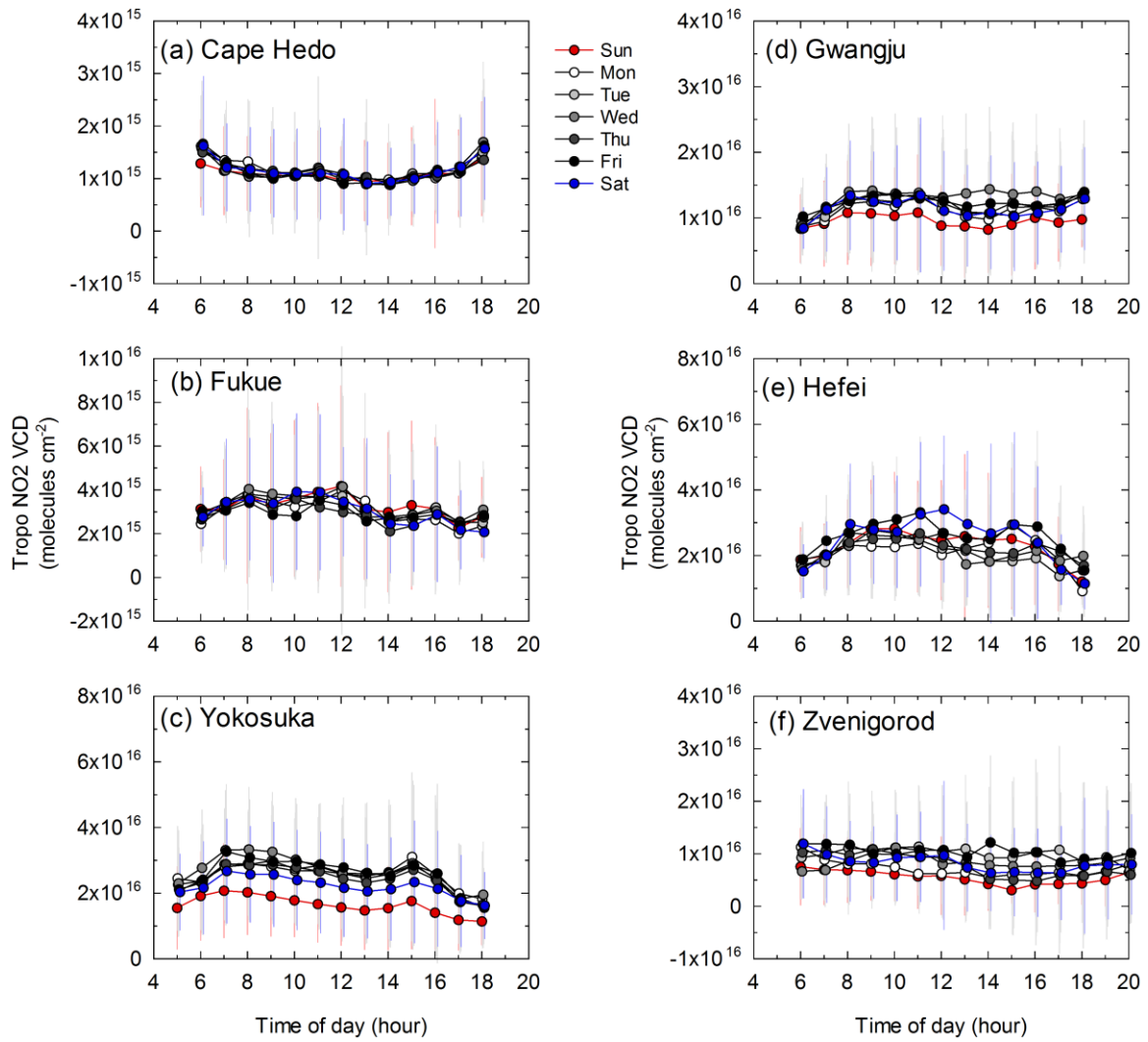
1024



1025

1026 **Fig. 14.** Comparison of average diurnal cycles of  $\text{NO}_2$  observed by MAX-DOAS at Yokosuka  
 1027 (partial columns in the lowest 1-km layer, colored circles) and by surface monitoring at  
 1028 Nagahama (near Yokosuka, pale colored lines) for (a) four selected months (January, April,  
 1029 July, and October) and for (b) weekdays and weekends. Error bars represent the  $1\sigma$  range of  
 1030 the included data (MAX-DOAS).

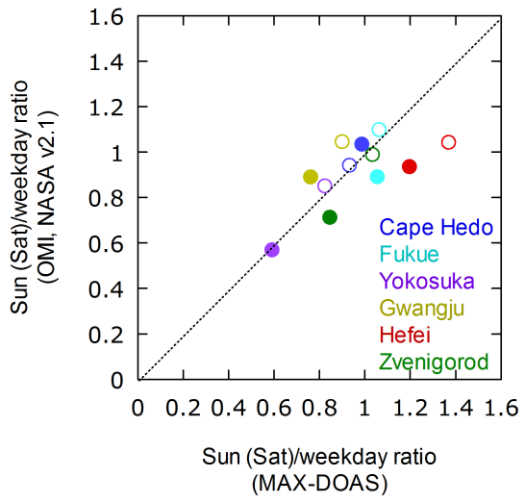
1031



1032

1033 **Fig. 15.** Diurnal variations in TropoNO<sub>2</sub>VCD separately averaged for days of the week. Error

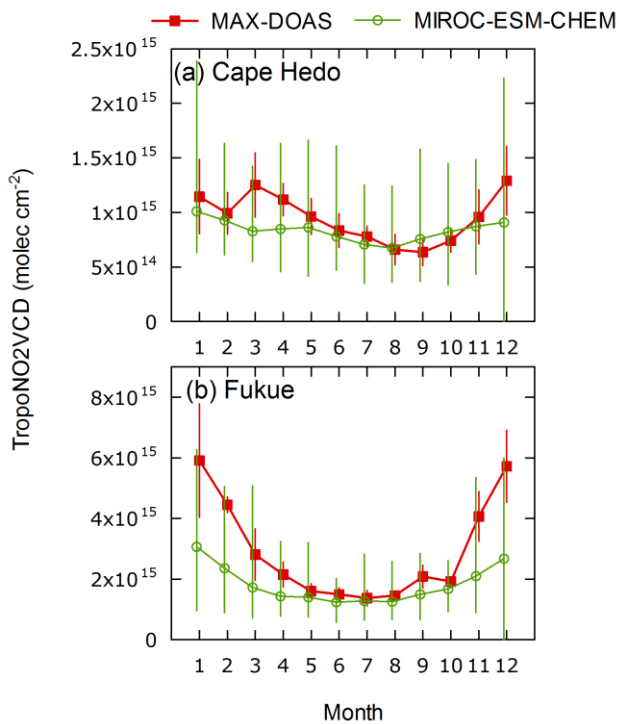
1034 bars represent the  $1\sigma$  range of the included data.



1035

1036 **Fig. 16.** Weekend reduction ratios for TropoNO<sub>2</sub>VCD derived from MAX-DOAS and OMI  
 1037 (using NASA ver. 2.1 algorithm). Open and closed symbol represent Saturdays and Sundays,  
 1038 respectively.

1039

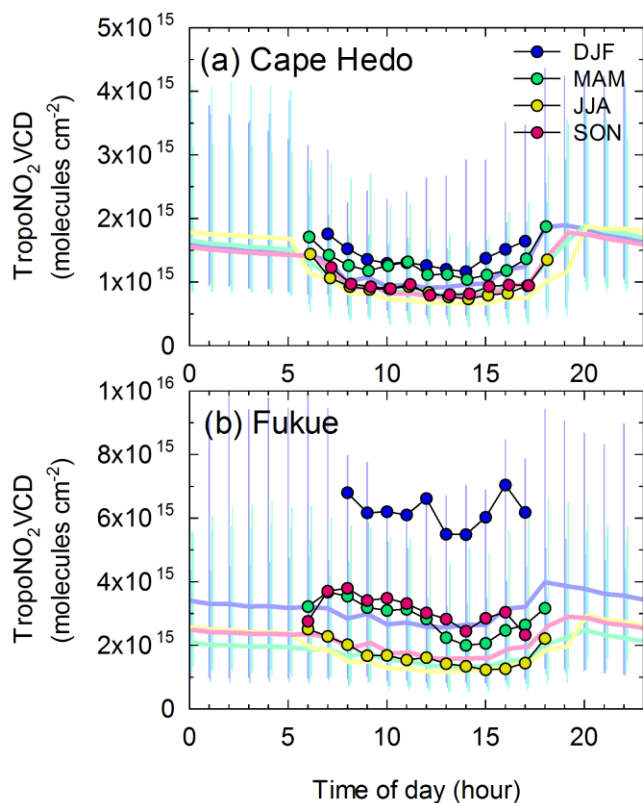


1040

1041 **Fig. 17.** Comparisons of average seasonal variations in TropoNO<sub>2</sub>VCD derived from  
 1042 MAX-DOAS observations and model simulations (MIROC-ESM-CHEM). Data from the  
 1043 hours of satellite observations (OMI) are used. Error bars for MAX-DOAS represent  
 1044 variations in the monthly averages over the studied years, whereas those for model  
 1045 simulations represent the full ranges of hourly averages included in each hour.

1046

1047



1048

1049 **Fig. 18.** Comparisons of average diurnal variations in TropoNO<sub>2</sub>VCD derived from  
 1050 MAX-DOAS observations (colored circles) and MIROC-ESM-CHEM model simulations  
 1051 (pale colored lines) for four seasons. Error bars for model simulations represent full ranges of  
 1052 hourly averages included in each hour.

1053

## 1054 **Supplementary Material**

### 1055 **Overview and Features of AOD**

1056 The methodology used to derive AOD values at 476 nm is described in the main text, and the  
1057 results are briefly summarized in this supplementary material. A color index (defined as the  
1058 ratio of the intensities at 500 and 380 nm) was used to screen out cloudy cases. The threshold  
1059 values used for the color index are listed in Table S1. The threshold value for Cape Hedo was  
1060 changed from 1.50 (Takashima et al., 2009) to 2.40 (this study) with equivalence, because the  
1061 offsets at the two wavelengths were newly taken into account for the revised calculation of  
1062 the color index. For other locations, we tentatively determined the equivalent color index  
1063 threshold values based on the assumption that the color ratio under conditions where the sky  
1064 was the most whitish was similar to that at Cape Hedo; this provided calibration information  
1065 for the relative responses of the individual instruments at 380 and 500 nm.

1066 Figure S1 shows the time series of monthly means of the AODs at six sites, with and  
1067 without cloud screening, based on the MAX-DOAS color index. The site-to-site differences  
1068 were not very large in comparison with those in the case of NO<sub>2</sub>; in particular, the AOD  
1069 levels for Yokosuka ( $0.24 \pm 0.05$  ( $1\sigma$ )) as averages of monthly mean values after cloud  
1070 screening, see Table S2), an urban site, were similar to those at Cape Hedo ( $0.33 \pm 0.13$  ( $1\sigma$ )),  
1071 a remote island. Hefei had the highest average value ( $0.59 \pm 0.13$  ( $1\sigma$ )) among the studied  
1072 locations. The levels were roughly comparable to the climatological AOD values derived  
1073 from satellite sensors, i.e., Moderate Resolution Imaging Spectroradiometer (MODIS)/Terra,  
1074 MODIS/Aqua, and Multi-angle Imaging Spectroradiometer (MISR)/Terra (Fig. S1 and Table  
1075 S2). The used monthly average satellite data are from MODIS/Terra (Collection 5) and  
1076 MODIS/Aqua (Collection 5.1) at a  $1^\circ \times 1^\circ$  grid resolution, and MISR/Terra (ver. 31) at a  $0.5^\circ$   
1077  $\times 0.5^\circ$  grid resolution, available from the NASA Goddard Earth Sciences Data and  
1078 Information Services Center (<http://daac.gsfc.nasa.gov/giovanni/>). For the MODIS sensors,  
1079 the AOD values at 550 nm were converted to those at 476 nm using the reported Ångström

1080 parameters. For MISR, the Ångström parameters were estimated from the reported AOD  
1081 values at multiple wavelengths (443, 555, 670, and 865 nm), and then the AOD values at 476  
1082 nm were estimated. Although the MODIS/Terra and MISR/Terra observations were made in  
1083 the morning, and the MODIS/Aqua observations were made in the afternoon, they were all  
1084 compared with the daytime averages of the MAX-DOAS observations. The AODs derived  
1085 from MAX-DOAS did not show significant diurnal variations (data not shown).

1086 Similar seasonal variation patterns at remote islands (Cape Hedo and Fukue) were found  
1087 for the MAX-DOAS and satellite observations, with higher values in winter–spring as a result  
1088 of long-range transport from the Asian continent along the westerlies. The agreement was  
1089 excellent for Zvenigorod. Common increases in August 2010 were attributable to intense  
1090 forest/peat fires. At Yokosuka, the average MAX-DOAS AOD level with cloud screening was  
1091 more consistent with MISR than with MODIS (especially in summer), partly because of  
1092 better spatial resolution. Similar tendencies were found for Gwangju and Hefei. For Hefei,  
1093 the month-to-month variation patterns were qualitatively similar for MAX-DOAS and  
1094 satellite data. Comparisons with satellite data with finer spatial resolutions will be studied in  
1095 the future.

1096 Figure S2 shows hourly-averaged AODs derived from MAX-DOAS and sky radiometer  
1097 (Aoki and Fujiyoshi, 2003) data at Fukue for 2009. The AOD value at 476 nm for sky  
1098 radiometer was calculated from the reported AOD value at 500 nm and the Ångström  
1099 exponent. A strong positive correlation was found around the 1:1 line. Similar comparisons  
1100 with sky radiometers and Mie lidar observations were successful at Tsukuba (Irie et al., 2008)  
1101 and at Cape Hedo (Takashima et al., 2009). Based on these features, we conclude that our  
1102 AOD products, with an estimated 30% uncertainty, are basically consistent with available  
1103 observations. As mentioned in the main text, 30% uncertainty in the AOD introduced only  
1104 10% or less uncertainty in the TropoNO<sub>2</sub>VCD. Therefore the aerosol information can be  
1105 satisfactorily used to estimate NO<sub>2</sub> optimally and to study the general trends in the



1106 OMI(NASA)/MAX-DOAS ratio of TropoNO<sub>2</sub>VCD against the AOD.

1107 **Table S1.** Recommended threshold values for color index used for cloud screening.

Instrument	Threshold value
Cape Hedo #1	2.40
Yokosuka #1	1.67
Fukue #1	0.81
Fukue #2	2.40
Fukue #3	1.55
Gwangju #1	2.20
Gwangju #2	2.10
Gwangju #3	2.02
Hefei #1	1.74
Hefei #2	2.01
Zvenigorod #1	1.57

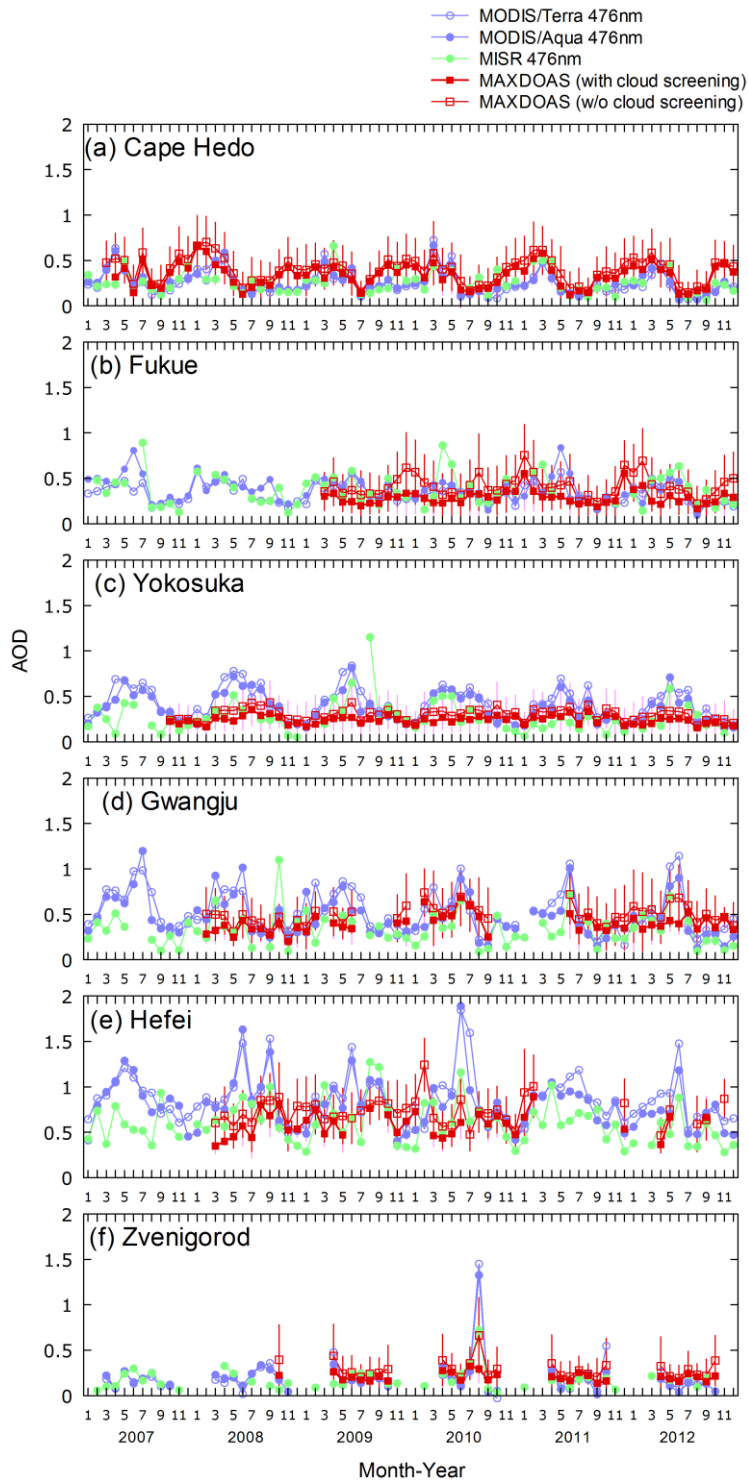
1108

1109 **Table S2.** Averages and  $1\sigma$  ranges of monthly mean AOD values derived from MAX-DOAS

1110 observations and satellite observations.

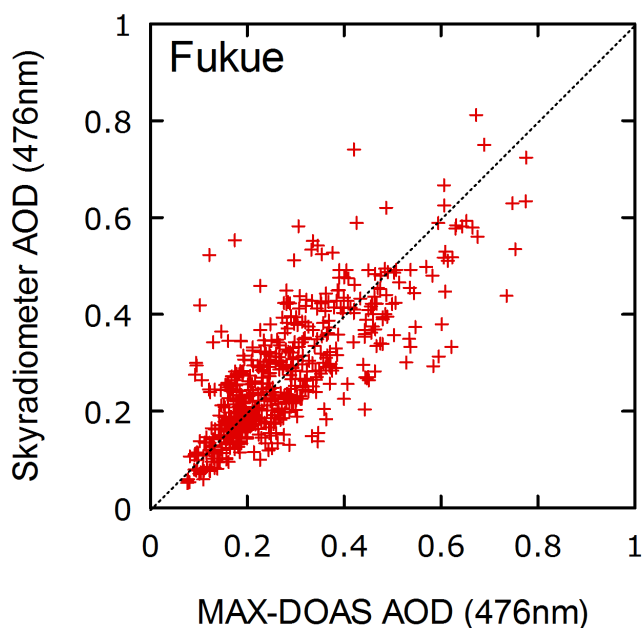
	MAX-DOAS (with cloud screening)	MAX-DOAS (without cloud screening)	MODIS/Terra	MODIS/Aqua	MISR/Terra
Cape Hedo	$0.33 \pm 0.13$	$0.40 \pm 0.14$	$0.26 \pm 0.13$	$0.25 \pm 0.14$	$0.26 \pm 0.12$
Yokosuka	$0.24 \pm 0.05$	$0.30 \pm 0.06$	$0.37 \pm 0.16$	$0.42 \pm 0.18$	$0.27 \pm 0.17$
Fukue	$0.29 \pm 0.08$	$0.42 \pm 0.12$	$0.38 \pm 0.14$	$0.34 \pm 0.12$	$0.37 \pm 0.17$
Gwangju	$0.40 \pm 0.10$	$0.50 \pm 0.11$	$0.47 \pm 0.23$	$0.53 \pm 0.23$	$0.33 \pm 0.18$
Hefei	$0.59 \pm 0.13$	$0.73 \pm 0.15$	$0.80 \pm 0.28$	$0.86 \pm 0.28$	$0.60 \pm 0.23$
Zvenigorod	$0.21 \pm 0.05$	$0.29 \pm 0.10$	$0.19 \pm 0.19$	$0.21 \pm 0.22$	$0.18 \pm 0.11$

1111



1112

1113 **Fig. S1.** Time series of monthly averages of AOD derived from MAX-DOAS and satellite  
 1114 observations. The satellite observations are derived using MODIS and MISR sensors on  
 1115 board Terra and Aqua. MAX-DOAS data, with and without cloud screening, are provided  
 1116 with error bars representing the  $1\sigma$  range of the included data.



1117  
 1118 **Fig. S2.** Scatterplot between AODs observed by MAX-DOAS and a sky radiometer at Fukue  
 1119 site in 2009.

1120

1121

1122 **References**

1123 Aoki, K, and Fujiyoshi, Y.: Sky radiometer measurements of aerosol optical properties over  
 1124 Sapporo, Japan. *J. Meteorol Soc. Jpn.*, 81, 493-513, 2003.

1125 Irie, H., Kanaya, Y., Akimoto, H., Iwabuchi, H., Shimizu, A., and Aoki, K.: First retrieval of  
 1126 tropospheric aerosol profiles using MAX-DOAS and comparison with lidar and sky  
 1127 radiometer measurements, *Atmos. Chem. Phys.*, 8, 341-350, 2008.

1128 Takashima, H., Irie, H., Kanaya, Y., Shimizu, A., Aoki, K., and Akimoto, H.: Atmospheric  
 1129 aerosol variations at Okinawa Island in Japan observed by MAX-DOAS using a new  
 1130 cloud-screening method, *J. Geophys. Res.*, 114, D18213, doi:10.1029/2009JD011939,  
 1131 2009.

1132